Laser Microfabrication of Porous Collagen Scaffolds for Biological Applications

Christina Yiannakou, M.Sc.

Master of Neuroscience

Medical School, University of Crete

Heraklion, Crete, Greece

October 2018

Supervisors:

Prof. Achille Gravanis, Medical School, University of Crete

Dr. Emmanuel Stratakis, IESL-FORTH

Dr. Dimitrios S. Tzeranis, IMBB-FORTH

Committee:

Prof. Achille Gravanis, Medical School, University of Crete

Dr. Emmanuel Stratakis, IESL-FORTH

Prof. Kiriaki Sidiropoulou, Department of Biology, University of Crete

Contents

Ευχαριστίες

Θα ήθελα ολοκληρώνοντας την πτυχιακή μου εργασία να ευχαριστήσω τους ανθρώπους που ήταν δίπλα μου και με στήριξαν.

Αρχικά τον καθηγητή μου καθ. Γραβάνη Αχιλλέα που μου έδωσε την ευκαιρία να εργαστώ στα εργαστήρια του ‘’Neural Tissue Engineering Lab’’ του ΙΤΕ και να εκπονήσω την πτυχιακή μου εργασία και πίστεψε στην προσπάθεια μου στηρίζοντας.

Ένα ιδιαίτερο ευχαριστώ στον επιβλέπον καθηγητή μου Δρ. Εμμανουήλ Στρατάκη για την εμπιστοσύνη που μου έδειξε όλα αυτά τα χρόνια, την υποστήριξή του και όλες τις ευκαιρίες που μου έδωσε. Ήταν απίστευτη χαρά για μένα να δουλεύω στο εργαστήριο του. Είμαι απίστευτα τυχερή που γνώρισα και συνεργάστηκα με ένα τέτοιο άνθρωπο και επιστήμονα. Η καθοδήγηση του και η βοήθεια του ήταν πολύ σημαντική για την επίτευξη της εργασίας αυτής. Τον θαυμάζω και θα είναι πάντα ο supervisor μου.

Θα ήθελα επίσης να ευχαριστήσω την καθ. Σιδηροπούλου Κυριακή για την ευκαιρία να βρίσκεται στην τριμελή επιτροπή μου και την ευκαιρία να επισκεφτώ το εργαστήριο Ηλεκτροφυσιολογιας της έστω για λίγο. Επίσης ένα τεράστιο ευχαριστώ στη καθ. Κυριακή Θερμός που ήταν σαν φως όλη τη χρονιά του μεταπτυχιακού όχι μόνο για μένα αλλά και για όλα τα παιδιά, έτοιμη να μας ακούσει και να μας φροντίσει.

Ακόμα θέλω να εκφράσω τις ιδιαίτερες ευχαριστίες μου και την ευγνωμοσύνη μου στο Δρ Τζεράνη Δημήτρη για την αμέριστη βοήθεια του και για όλες αυτές τις γνώσεις που μου χάρισε απλόχερα. Είμαι τυχερή για τα νέα πεδία που με δίδαξε και τις ενδιαφέρουσες συζητήσεις που είχαμε. Συζητήσεις με γνώση και γέλια. Πίστεψε σε εμένα και με στήριξε σε όλη τη διαδικασία της μεταπτυχιακής μου εργασίας. Είναι ένας σωστός άνθρωπος και καταπληκτικός επιστήμονας. Όσα και να πω θα είναι λίγα. Είμαι πολύ τυχερή που συνεργάστηκα μαζί του και έμαθα τόσα πράγματα. Χωρίς την βοήθεια του η πραγματοποίηση του στόχου μου θα ήταν σίγουρα δύσκολη. Ευχαριστώ.

Θα ήθελα να ευχαριστήσω την Αλέκα Μανουσάκη για τη συνεχή βοήθεια της και υπομονή της με τις μετρήσεις (SEM) των δειγμάτων μου αλλά και τις ευχάριστες συζητήσεις που είχαμε όλο αυτό το καιρό. Ένα θερμό ευχαριστώ στο Στέφανο Παπαδάκη για τη στήριξη τους σε ότι χρειαζόμουν στο εργαστήριο SEM.

Ευχαριστώ πολύ όλα τα παιδιά του εργαστηρίου για το ευχάριστο κλίμα συνεργασίας που πρόσφεραν σε όλη αυτή τη διάρκεια προσφέροντας μου όμορφες φιλίες και όμορφες στιγμές.

Ιδιαίτερα ευχαριστώ το Γιώργο Ζιάκα που με βοήθησε σε όλα τα βιολογικά πειράματα. Μου έμαθε τεχνικές που δεν γνώριζα και ήταν πάντα πρόθυμος να με βοηθήσει. Η συνεισφορά του στο βιολογικό κομμάτι είναι ανεκτίμητη. Μοιράστηκε τις γνώσεις του και μου χάρισε μια άψογη συνεργασία. Ήταν εκεί όποτε τον χρειαζόμουν. Επίσης θέλω να ευχαριστήσω την Όλγα Σαρλίδου που επίσης με μεγάλη χαρά με βοήθησε στην εκπλήρωση των βιολογικών πειραμάτων και ήταν πρόθυμη να απαντήσει σε κάθε ερώτημα μου. Περάσαμε όμορφες στιγμές.

Ένα ευχαριστώ σε όλους μου τους φίλους για την αντοχή που έδειξαν απέναντι μου στις δύσκολες στιγμές και για την εμψύχωσή που μου χάριζαν όταν το είχα ανάγκη. Ειδικότερα τους Πέγκυ, Νεκταρία, Αργυρώ, Ιωάννα, Αντωνία, Γιώργο και Μάκη που ήταν πάντα εκεί για έμενα κάνοντας αυτό το ταξίδι ακόμα πιο όμορφο. Ευχαριστώ τον Άχμεντ που με στηρίζει και πιστεύει σε όλο αυτό που κάνω ακόμα και όταν δεν το πιστεύω εγώ. Τον ευχαριστώ που ήταν πάντα εκεί να μου δίνει ανάσες όταν τις χρειάζομαι.

Ένα μεγάλο ευχαριστώ στους νονούς μου Πάμπο και Μαρία για τη συνεχή ψυχολογική υποστήριξη όταν όλα έμοιαζαν δύσκολα. Ήταν δίπλα μου σε κάθε στιγμή και έτοιμοί να με ακούσουν και να με βοηθήσουν. Τέλος θέλω να ευχαριστήσω πραγματικά τους γονείς μου Χαράλαμπο και Σοφία, τις αδερφές μου Ελένη και Βασιλική, τη μικρή Σοφία (το Δρακάκι μου) αλλά και το Νίκο για τη συμπαράσταση που απλόχερα μου έδιναν όλα αυτά τα χρόνια. Πίστευαν πάντα σε εμένα και με στήριζαν σε κάθε μου απόφαση. Το μεγαλύτερο ευχαριστώ για την υπομονή τους αλλά και την εμπιστοσύνη που μου έδειχναν σε κάθε μου επιλογή. Πάντα στο πλάι μου με αγάπη θυμίζοντας μου πόσο όμορφο είναι αυτό το ταξίδι. Χωρίς τη στήριξή τους δεν θα ήταν τίποτα υλοποιήσιμο. Τους ευχαριστώ για όλα και τους αφιερώνω την εργασία αυτή για όλη την ανιδιοτελή στήριξη. Ευχαριστώ.

List of Abbreviations

2D	Two-Dimensional
3D	Three-Dimensional
ALS	Amyotrophic Lateral Sclerosis
CAD	Computer-Aided Design
CAM	Computer-Aided Manufacturing
CFP	Collagen Gel Photomodification
CG	Collagen – Glycosaminoglycan
CNC	Computer Numerical Control
DHT	Dehydrothermal
DMEM	Dulbecco's Modified Eagle Medium
ECM	Extracellular Matrix
FBS	Fetal Bovine Serum
GAG	Glycosaminoglycan
CG	Collagen-GAG
ITS	Insulin – Transferrin – Selenium
PCS	Porous Collagen-Based Scaffolds
SEM	Scanning Electron Microscopy
STL	Surface Tessellation Language
fs	Femtosecond (10^{-15} s)
ps	Picosecond (10^{-12} s)
ns	Nanosecond (10^{-9} s)
µm	micrometer (10^{-6} m)

List of Figures

List of Tables

Abstract

A basic part of bioengineering is the materials. Materials are what enable us to cultivate and control cells various functions. This has two basic applications, Regenerative medicine and 3D culture. The goal of this field is to find treatments for some injuries or organs that have suffered some damage. According to the literature, materials seem to have helped in the accomplishment of this. What interests us in this work is to make 3D scaffolds - tissue models and understand how the cell's environment affects its function. There is a wide range of materials, but we are interested in Porous Scaffolds based on Collagen. It has a biological activity and low antigenicity. Because of its pores, cells enter and bind to the material. The way they interact with the environment affects their behavior. The environment affects the way of their outgrowing, orientation, organization and interactions with each other. Also affects the way they interact with other type of cells. Collagen based scaffolds have some limitations in size and construction. Here's where the lasers come, which allow us to make structures with high precision, complex shapes and in the scale of micrometers. In this way we can build structures and shapes and control how the environment that perceives the cell affects it. Specifically the aim of the present work is the creation of 2D and 3D structures, their characterization and in vitro experiments with motor neuron and muscle cells. At the level of structures the characterization can be done with SEM images, mechanical collagen resistance and, SHG microscopy. Then in the in vitro experiments we will construct such structures that will study the response of co culture of motor neuron and muscle cells. The goal, ‘’the dream’’ is to be able to build structures with direct application to clinical regenerative medicine and in vivo trials. A field in which we have to overcome a lot of but one step at a time.

Περίληψη

Ένα βασικό κομμάτι της Βιοτεχνολογίας είναι τα υλικά. Τα υλικά είναι αυτά που μας επιτρέπουν να καλλιεργήσουμε και να ελέγξουμε τις διάφορες λειτουργίες τους. Αυτό έχει δύο βασικές εφαρμογές. Την αναγεννητική ιατρική και τις 3D καλλιέργειες. Αυτό το πεδίο θέλει να βρει θεραπείες για κάποια τραύματα ή κάποια όργανα που υπέστη κάποια βλάβη ή ακόμα και για κάποιες ασθένειες. Σύμφωνα με τη βιβλιογραφία φαίνεται ότι τα υλικά βοήθησαν να δουλέψει αυτό. Αυτό που μας ενδιαφέρει στη παρούσα εργασία είναι να φτιάξουμε ικριώματα- μοντέλα ιστών και να καταλάβουμε πως το περιβάλλον του κυττάρου επηρεάζει τη λειτουργία του. Υπάρχει ένα ευρύ φάσμα υλικών, εμάς όμως μας ενδιαφέρει να ασχοληθούμε με τα Πορώδη Ικριώματα με βάση το Κολλαγόνο. Σύμφωνα με τη βιβλιογραφία αυτά τα υλικά έχουν αποδεδειγμένη κλινική χρήση στην αναγεννητική ιατρική και όπως φαίνεται το μέγεθος πόρων επηρεάζει την αναγέννηση. Ο τρόπος με τον οποίο αλληλοεπιδρούν με το περιβάλλον επηρεάζει τη συμπεριφορά τους. Τον τρόπο ανάπτυξης, προσανατολισμούς, οργάνωσης και αλληλεπιδράσεις μεταξύ τους άλλα και με άλλο είδος κυττάρων. Τα ικριώματα με βάση το κολλαγόνο έχουν κάποιους περιορισμούς όσο αφορά το μέγεθος και τη κατασκευή τους. Εδώ είναι που έρχονται τα λέιζερ τα οποία μας επιτρέπουν να κάνουμε δομές με μεγάλη ακρίβεια, περίπλοκα σχήματα και στη κλίμακα των μικρομέτρων. Με αυτό λοιπόν τον τρόπο μπορούμε να φτιάξουμε δομές και σχήματα και να ελέγξουμε πως το περιβάλλον που αντιλαμβάνεται το κύτταρο το επηρεάζει. Συγκεκριμένα ο σκοπός της παρούσας εργασίας είναι η δημιουργία 2D και3D δομών, ο χαρακτηρισμός τους και in-vitro πειράματα με συγκαλλιέργειες από κινητικούς νευρώνες και μυϊκά κύτταρα. Στο επίπεδο δομών ο χαρακτηρισμός μπορεί να γίνει με εικόνες SEM, μηχανικές αντοχές του κολλαγόνου και, SHG μικροσκοπία. Στη συνέχεια στα in-vitro κομμάτια θα φτιάξουμε τέτοιες δομές που θα μελετήσουμε την απόκριση δύο ειδών κυττάρων: κινητικούς νευρώνες και μυϊκά κύτταρα. Ο στόχος, είναι να μπορέσουμε να φτιάξουμε δομές με άμεση εφαρμογή στην αναγεννητική ιατρική και στις κλινικές in-vivo. Ένα πεδίο στο οποίο έχουμε να ξεπεράσουμε πολλά, με ένα βήμα την φορά.

Chapter 1: Introduction

This thesis describes a novel laser-based method for high-precision 3D microfabrication of porous collagen-based scaffolds, similar to biomaterials utilized clinically in regenerative medicine. This chapter introduces the reader to the motivation and impact of this study, presents the current state of the art and summarizes the context of the following chapters.

1.1. Introduction

Researchers have long tried to understand cell function, find ways to control key functions of various cells, and utilize this knowledge in key applications: understand the molecular basis of disease, create diagnostic devices, find diseases treatments, engineer *in vitro* tissue models and develop novel treatments for organ regeneration. For example, in order to address the need to replace injured organs, the field of regenerative medicine develops treatments by integrating the fields of materials science, chemistry and biology. Since the early findings in the 1970s that porous collagen-based scaffolds (PCS) can induce regeneration in severe skin injuries [1] the field of regenerative medicine has advanced significantly. Contemporary interdisciplinary approaches combine biomaterials, drugs and stem cells in order to develop effective treatments for more kinds of organs. A large part of biomaterial development focuses on providing new materials that can overcome the short-comings of existing ones [2]. In general, biomaterials used *in vitro* and *in vivo* studies should have some basic characteristics: They should be biocompatible, induce low toxicity or infection to cells, their degradation rate should be optimized (e.g. slow enough to allow seeded cells to grow and function normally), and ideally should provide clues that can guide cells towards the formation of functional novel tissue *in vivo* [3].

The development of biomaterials with appropriate topographical features is a crucial step towards providing favorable environment to cells. Porous Collagen-GAG Scaffolds (PCS), also known as "artificial skin", have been used in variety researches as a tissue scaffold that allows for fast host regeneration. Collagen–GAG (CG) scaffolds ability to induce regeneration in severe skin injuries was reported by Yannas and Burke [4]. Since then CG scaffolds have been extensively used for skin cell growth and wound coverage. PCS (CG scaffolds is a subset of PCS) are scaffolds-like biomaterials fabricated by the freeze-drying (lyophilization) method. The mean pore diameter of PCS (20 – 400 μm) is relatively large compared to cell size (10-20 μm). PCS first received FDA approval for the treatment of severely injured skin and peripheral nerves in 1980s and 1990s respectively (marketed as Integra DRT® and Neuragen® respectively). Since then, several companies have developed similar collagen-based scaffold sheets for the treatment of skin injuries, burns or for cosmetic surgery. A disadvantage of PCS is that due to their solid state and size, their application as a graft requires a surgery. Their advantages include their proven biological activity and low antigenicity. Furthermore, due to the size of their pores, cells can enter and bind to the material, providing them a 3D microenvironment. For this reason, 3D culture of cells inside PCS has been proposed to provide several advantages over established two-dimensional cultures, as a PCS can better mimic the extracellular matrix of a tissue. The way they interact with the environment affects their behavior. These advantage made them an effective material in the field on biological applications research.

By modulating the key physicochemical properties of PCS (mean pore diameter, mass fraction, degradation rate, chemical composition, and surface chemistry) it is possible to provide cells tunable biochemical and physical cues (e.g. topographical and mechanical), a major advantage in the field of biomaterials. Cells respond to their *in vivo* insoluble microenvironment by initiating a sequence of different processes including the change of cellular functions and shape [5]. The effect of topographical cues, dictated also by a geometrical discontinuity or anisotropy, on cellular shape has been known for many years and the phenomenon is termed as contact guidance [6]. Various approaches have been evaluated in order to define topographical cues provided to cells, using various kinds of materials such as polymers, ceramics or metals, and fabrication techniques including photolithography, electrospinning and laser structuring [7]. Patterning of different topographic clues has been shown to affect key cell functions including outgrowth, orientation and differentiation. Topographic clue patterning can assist in better understanding many biological processes by better mimicking *in vivo* structures. Towards this goal, several approaches have been investigated to pattern in three dimensions (within a material volume) or two dimensions (on the top of a surface) and develop 3D matrix analogs that will guide cells towards desired phenotypes. Such biomaterials can also be utilized to develop advanced in vitro culture systems that can enable the precise control and study of cell–cell interactions by better mimicking the complexity of *in vivo* cell microenvironments [8]. A less investigated topography, comprising morphological features at various length-scales, can be provided in PCS via laser fabrication techniques.

1.2. Motivation

1.2.1. The Role of ECM Architecture in Cell and Tissue organization

Living tissues are intricate ensembles of multiple cell types embedded in a complex, well-defined extracellular insoluble matter, the extracellular matrix (ECM). ECM is a collection of extracellular molecules secreted by cells, a heterogeneous chemical composite made of multiple structures that provide structural and biochemical support to tissue cells. ECM usually consists of an interconnected network of macromolecules, fibrous proteins (e.g. collagen and elastin) and a largely amorphous inter-fibrillary matrix (glycosaminoglycans, cell-binding adhesive glycoproteins, proteoglycans and water). Tissue structure, critical for its function, is regulated by interactions between cells and their surrounding ECM [9]. ECM also serves as a reservoir of soluble factors (e.g. growth factors, hormones, cytokines) that influence and regulate tissue structure and function [10]. All these constituents (cues) of the physiological milieu are not randomly distributed in living tissues. Instead, the location of each constituent is accurately defined by the tissue architecture and results in dramatically inhomogeneous microenvironments. Many ECM proteins follow a hierarchical assembly pattern, providing morphogenic cues to control cell survival, proliferation, migration, polarization, and differentiation [10]. Therefore, it's important to understand the role of ECM in order to develop biomaterials, to a view of ECM as an integral determinant of tissue specificity itself. As such, organ structure and consequently organ function are determined by the dynamic and reciprocal interactions between the organ’s constituent tissues, the structure and function of which are determined by the dynamic and reciprocal interactions between the cells and ECM comprising a given tissue [11]. Form large-scale structures up to several hundred μm in size that interact with multiple individual cells to coordinate complex multicellular behavior has developed. In biological tissues, cells and microenvironmental cues are integrated and organized according to tissue-specific *in vivo* 3D histoarchitecture. 3D scaffolds, including PCS, could behave similarly to corresponding tissues and could be used in therapeutic applications (regenerative medicine) or as realistic tissue models [12].

1.2.2. Emerging Methods for Engineering Complex 3D Cellular Microenvironments

Functionality of tissues arises, apart from its components (cells and ECM molecules), from their location of those components relative to each other. Several published approaches have attempted to re-*create in vitro* the cell-tissue 3D histoarchitecture observed *in vivo*. In order to study the effect of complex topographical features of 3D cellular microenvironments in various tissues, researchers use scaffolding molecules of natural or synthetic origin to support cell growth. The microenvironment of a cell comprises of all cues affecting cells, such as attachment to neighboring cells, attachment to ECM molecules (e.g. via integrins) and molecules secreted by the cell itself or by other cells [12]. The well-established 2D cell culture on flat and rigid substrates, a common laboratory technique since the 1950s, has elucidated fundamental principles in cell biology [13], however it cannot recapitulate the complexity of the topographical milieu of cells sensed in 3D tissues. This limitation lead to the development of techniques for 3D cell culture inside biomaterials, including porous scaffolds. A large variety of biomaterials including natural, synthetic and their combinations have been reported during the last two decades [14]. Bio-mimetic material development has focused on generating materials with similar structures and chemical composition as the ECM of the organ of interest [15]. For example, in order to mimic the composition of skin, whose ECM is reach in glycosaminoglycans (GAGs), GAGs are frequently added to a collagen-rich matrix. The bottom layer of the bilayer artificial skin invented by Yannas and Burke was made of collagen/chondroitin-6-sulfate coprecipitate which functions as a dermal regenerating template [16].

Approaches of 3D cellular microenvironment in tissues of mimic tissue, differ in the type of porous material used as the scaffold, inside which cells are cultured. Some techniques use synthetic polymers while others use natural biopolymers such as collagens or elastin, harvested from tissues, either in solution or as 3D structures. In this study we demonstrate a method for fabricating hierarchical structures based on ultrafast laser ablation of Porous Collagen Scaffolds, a straight-forward technique that takes place in room temperature. This thesis shows that laser ablation provides a novel 3D manufacturing process that can realize different textured surfaces and all material structuring. The fabricated surfaces have been used as culture substrates for culturing several kinds of cells including cell lines (C2C12, NSC34) and stem-cell derived neurons.

1.3. Literature Review

This section summarizes key features of porous collagen scaffolds and reports the current state of the art on biomaterial microfabrication by laser ablation.

1.3.1. Porous Collagen-Based Scaffolds

Porous Collagen-based Scaffolds (PCS) are among the most important biomaterials available today due to their established clinical application in regenerative medicine. PCS are fabricated in dry solid state by lyophilizing appropriate suspensions whose main chemical component is collagen. Lyophilization is a method of dehydration that can provide scaffolds of homogenous pore structure. PCS are fabricated by freeze-drying a suspension of micro-fibrilar collagen I (0.5% to 5% w/v) in 0.05 M acetic acid. CG scaffolds, originally developed for skin regeneration, have demonstrated great potential for bone tissue engineering due to their ability to promote cell growth and tissue development [17]. Previous studies in animal models of skin regeneration suggest that there is a critical range of mean pore diameter (as 20-120 μm) for optimal regenerative activity [3]. Modifications of the lyophilization process result in the production of scaffolds of mean pore sizes ranging from 85 μm to 325 μm. CG scaffolds have been used to study the effect of the mechanical environment on the contractile response of fibroblasts [18]. The permeability of CG scaffolds as a function of pore diameter was characterized using experimental and mathematical modeling techniques [19]. Researchers investigated *in vitro* tendon cell-mediated contraction of two kinds of cross-linked CG matrices [20]. Type I CG matrix was evaluated in tendon defects, while a CG scaffold made of type II collagen was evaluated for treating articular cartilage defects. All type I matrices were cross-linked by dehydrothermal (DHT) treatment prior to any additional chemical or physical cross-linking. Scaffolds made of type I and II collagen were cross-linked by UV illumination. Type I CG scaffolds can induce partial regeneration of organs in the adult mammal according the results on the ligand's binding of fibroblasts to the collagen surface, the mean pore size and the degradation [21]. Proper selection of the heat-transfer parameters during the freezing results in scaffolds of homogenous mean pore diameter, usually in the range 50 to 100 μm, but as small as 10 μm [22].

1.3.2. Laser Microfabrication of Biomaterials

The combination of laser light monochromaticity and controlled pulsed excitation opens up the possibility of highly selective narrow-band excitation and high temporal resolution that has enabled several applications relevant to tissue engineering. Methods for 3D microfabrication of biomaterials are discussed in many reviews. In the vast majority, such studies utilize collagen gels rather than PCS, the biomaterial of interest in this study [23]. A study on 3D micropatterned fabrication of collagen gels by femtosecond laser ablation (800 nm, 45 fs Ti:Saph.) focused on the effects of laser fluence and exposure time on the size and morphology of the resulting ablation patterns, such as the holes, lines and grids [24]. It showed the effect of laser fluence on the rage of the pattern and the result of the adhesion. Porous scaffolds sculpted by laser ablation in the intermediate fluence regime resulted in good adhesion and growth by rat bone marrow mesenchymal stem cells and human fibroblasts. A 2010 study investigated the photophysical mechanisms of collagen gel photomodification (CFP) by a fs Ti:Saph laser (780 nm, 80 MHz repetition rate, 120 fs pulse width) and demonstrated that CFP can be used for bending and cutting collagen fibers and creating 3D patterns within a collagen gel with ~2 μm precision [25]. CFP and imaging were performed using a laser scanning microscope coupled to a Ti: Saph laser. Collagen fiber structure degradation was possible by laser pulses of 0.1-0.5 nJ energy. The same study also managed to fabricate interconnected channels of width <2 μm inside the collagen gel. Laser ablation of collagen gels by a two-photon absorption procedure (830 nm, 400 mW average laser power) was used to generate 3D microtracks in dense 3D structures that support and guide collective cancer cell invasion, and channels of 150 μm length whose widths and depth range within 3-30 μm in x and z directions [26]. A combination of laser ablation with a Ti: Saph laser and subsequent imaging by a two-photon microscope was used on acellular collagen gels to create cavities [27]. The effect of laser wavelength (760 nm to 920 nm, 198 mW average laser power) on collagen was investigated. Results showed that the diameter of the photodamaged region was directly correlated to average laser power. The main optical and material features of the above studies are presented in **Table 1.3.2-1**.

Despite a large number of the previous studies on different solid materials and on collagen gel, many questions are still open in the field of ultrashort laser interactions with porous collagen scaffold. This is the state of the art of this project as it will be shown in paragraphs below [1.4].

Reference	**Biomaterial**	**Ablation Features**	**Optical Features**
[23]	2 mg/mL collagen I gel	**Outer rim:** 5–10 μm wide / Raised from surface: 15 μm/ Depth: 50–100 μm. **Parallel Grooves:** 60μm long, 70 μm wide, 95 μm spacing.	λ = 800 nm, f_p =1 kHz, τ_p=45fs, E_p =2 mJ, U =100mm/s. **Damage Threshold:** 0.062J/cm^2 (Circular:5.0mJ/pulse, Lines:7.0mJ/pulse, Grid:5.0 mJ/pulse)

[27]	6 mg/ml collagen I gel	Length: 150µm Widths: 3µm Depths: 30 µm	λ =830 nm, P = 400 mW
[28]	Collagen Gel	**Channels Widths**: <2µm	λ =780 nm, f_p =80 MHz, P = 6 to 60 mW, τ_p =120 fs, E_p = 0.1 to 0.5nJ
[29]	Type I-A collagen gel	Submicron nodules at **depth**: 2-15-30 µm. **Size** formed: <1µm	λ =775 nm, τ_p =80 fs, f_p = 82 MHz, I = 60 mJ/cm^2
[30]	Collagen gel	damage 0 :st1 2nd: 1.74 µm and 0.86 µm . :nd339.8 µm and 31.2 µm	λ =760 to 920 nm, P =5,198 and 350 mW, τ_p =140fs, f_p =80MHz
[31]	Collagen gel	**Outer rim:** 5–10 µm wide / Raised from surface: 15 µm/ Depth: 50–100 µm. **Parallel Grooves:** 60µm long, 70 µm wide, 95 µm spacing.	I = 60 mJ/cm^2
[32]	Collagen-nanorod Hydrogels	resolution patterns: 8.7 ± 0.5µm 56.7 ± 3.0µm 128.6 ± 9.3µm 179.3 ± 23.5µm.	near-infrared (NIR) P =100, 150, 185 or 290mW, U = 0.25, 0.75 and 2.0 mm/s
[33]	Collagen and Type-B gelatine film		λ =790 nm, τ_p =60 fs, f_p = 11 MHz, E_p = 45 to 80 nJ. I = 40 or 400 mJ/cm^2
[34]	Collagen Scaffolds		λ =775 nm, P =2.5 W, τ_p =150 fs, f_p = 3 kHz.

Table 1.3.2-1: Summary of previous reports of generation of specific features by laser ablation. Where λ is the wavelength of laser, P is the Power of laser, Ep represent the power Energy τ_p is time of pulses and f_p is laser fluence of laser.

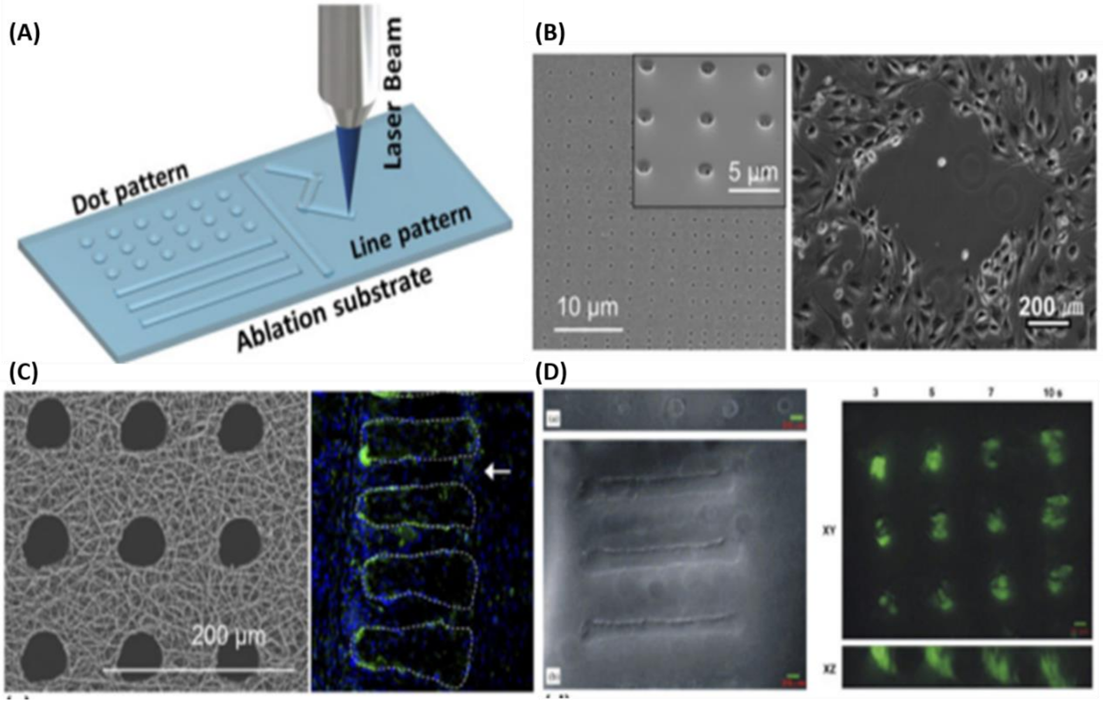

Figure 1.3.2-1 : Laser direct-writing ablation lithography. (A) Schematic of laser ablation for selective biomaterial removal; (B-C) Fabrication of nanoscale craters by laser ablation lithography, which could generate a repellent cell patterning. Magnification. (D) Fabrication of micro-holes in an electrospun fibrous scaffold via laser ablation; (E) DIC image of circular and line patterns generated by laser ablation onto the collagen hydrogel surface. The viability of seeded mesenchymal stem cells was confirmed via a fluorescent viability assay. [23]

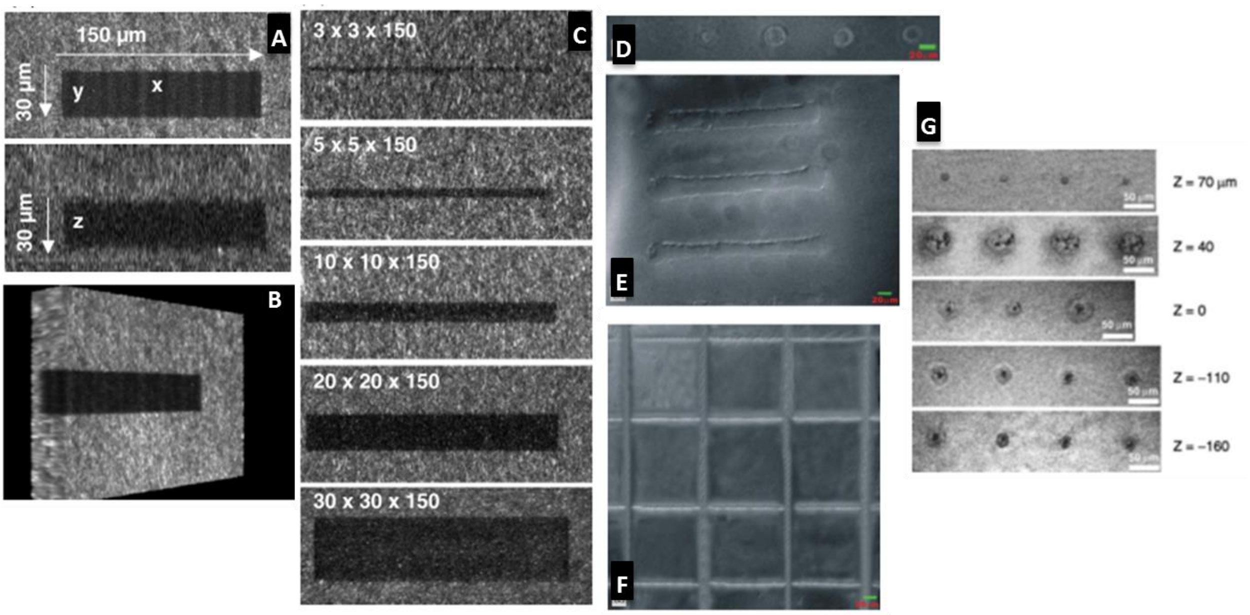

Figure 1.3.2-2: Two-photon laser generation of collagen-ablated microtracks within a 3D matrix. (A) x-y and x-z views of a two-photon laser-generated microtrack showing a collagen-cleared lumen. (B) 3D reconstruction of a laser-generated microtrack. (C) Collagen-ablated microtracks of different calibers. Circular craters (D) were produced by 2 s exposures of a pulsed laser of $E_p = 5$ mJ/pulse. (E) Lines produced by a pulsed laser of $E_p = 7$ mJ/pulse. (F) A grid pattern produced by a pulsed laser of $E_p = 5$ mJ/pulse moving at $U = 100$ µm/s. (G) Morphology of the ablation features at different locations of the laser focus. Positive z corresponds to the focus above the surface. Figures A-C are from [28]. Figures D-G are from [29].

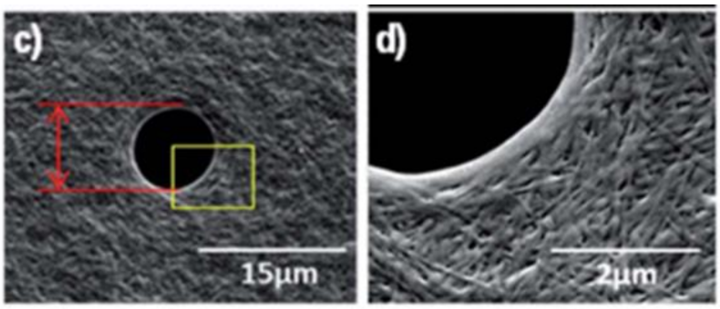

Figure 1.3.2-3: SEM image of a laser-fabricated cavity (left) obtained at resonance wavelength (800 nm). Right: magnified SEM image (highlighted area in left) showing the banding periodicity along the border of the cavity and surrounding areas of the laser irradiated site. [27].

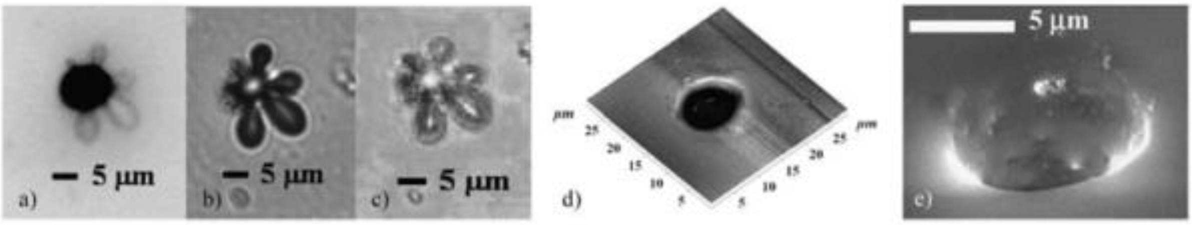

Figure 1.3.2-4: Irradiated zone of a gelatin film (Fluence=0.286 Jcm^{-2}, N=1375000 pulses). Optical micrographs of the same irradiated zone in (a) reflection, (b) transmission and (c) Z-scan modes. Micrographs of the crater formed in the film obtained by (d) SFM and (e) ESEM. From [30].

1.3.3. Applications of Laser Microfabricated Biomaterials

By exploiting the innovative technique of laser ablation and a proven clinical of porous collagen scaffold, it is possible to fabricate structures and shapes for different biological applications. The geometry of ECM, for example, is essential to modulate cell function and polarity and with this method we can fabricate geometries helping cell functions.

Recently, new biofabrication techniques have emerged, including microfabrication and photopolymerization, 3-D printing, microfluidics, and photochemistry. These tools enable to precisely construct controllable tissue models that can be used *in vitro* and mimic the *in vivo* 3D architecture of specific tissues. [31]. In an effort to develop complex scaffolds structures that better match natural tissue structure [27] has been developed, that use laser ablation and PCS. Correlating approaches of laser ablation and fabrication with (bio)materials, like porous collagen scaffold, seems to give selectively removes (bio)materials with high precision to create holes, lines and/or any other figures at micro/nano-scale [32]. Through these laser assisted (bio)fabrication technologies and the control of the spatial arrangement of (bio)materials at the resolution of 10 µm, lead into the fundamental understanding about cell-cell and cell-biomaterial interactions, which can be applied to regenerative medicine. With the appearance of ultra-short pulses laser systems, extremely new technology became accessible thus allowing laser treatment of practically various materials. As a result, extremely precise processing techniques are under developed with femtosecond laser marking and machining are thus used in optics, photonics, counterfeiting, ophthalmology and other fields [6].

1.4. Thesis Objective

The objective of this thesis is to provide the foundations for a novel laser-based method for microfabricating porous collagen-based scaffolds. It can be organized into three main tasks

- Characterization of PCS ablation by femtosecond lasers. Specifically, quantify ablation volume size as a function of key optical parameters (laser power) and manufacturing properties (machining speed, depth where ablation takes place inside scaffold). Interpret experimental results using simple analytic models.
- Develop a pipeline that enables the successful fabrication of complex components given an initial piece of PCS and the 3D drawing of the component to be fabricated.
- Utilize laser microfabricated PCS in pilot in vitro experiments in order to demonstrate the ability to control cell function by fabricating specific µm-sized features.

1.5. Thesis Outline

Chapter 1 reviews the objective and motivation of this thesis and provides background literature. Chapter 2 provides experimental characterization of fs laser ablation of PCS and a simple analytic model that is utilized to interpret them. Chapter 3 presents the pipeline utilized for practical implementation of 3D microfabrication in PCS. Chapter 4 presents small pilot *in vitro* studies that highlight the potential biological applications of microfabricated PCS. Finally, Chapter 5 summarizes the work and provides ideas for future work.

Chapter 2: Characterization of Laser Ablation in Porous Collagen Scaffolds

No prior study has focused on describing in detail the ablation of PCS by ultrafast lasers. Chapter 2 provides a detailed characterization of this process, a key prerequisite for engineering manufacturing systems that will utilize laser ablation to fabricate novel scaffolds of complex shape and structure. Section 2.1 provides theoretical background on the process of material removal by laser ablation. Section 2.2 analyze laser ablation's characteristics based on the theoretical background. Section 2.3 includes a description of the experimental setups utilized in this study for surface structuring, sample preparation and characterization, giving results in Section 2.4 and 2.5.

2.1. Introduction

2.1.1. Laser Ablation Physics

Laser fabrication is one the most promising emerging technologies for fabricating novel biomaterials. This section describes the fundamental physics of laser propagation, light-matter interaction, and material removal via laser ablation.

Previews studies have shown that the interaction of laser light with matter can induce permanent changes in the material's properties [30]. Surface modification of materials via laser light depends on several laser parameters including pulse energyE_p, pulse duration τ_p and pulse repetition rate f_p. It requires the deposition of a certain amount of energy which is absorbed by the material. Depending on the density, kinetics and localization of deposited energy, different kinds of surface modification can be achieved. Laser pulse duration is an important parameter in the ablation process. Indeed, several studies probed the interaction of pulsed lasers whose pulse duration τ_p lies in the femtosecond (fs), picosecond (ps) and nanosecond (ns) regime. Ultrafast pulses (fs) are characterized by very high peak intensities and their interaction with materials takes place within a timescale faster than lattice disorder and heat diffusion **Figure 2.1.1-1**. Lasers of ns pulses have larger heat-affected zones and shock waves compared with ps and fs pulsed lasers. The main differences between them are due to the mechanism of laser-induced target material removal processes. The fabrication of hierarchical structures by ablation via fs lasers has been previously described [33]. During fs laser ablation, plasma is produced after each laser pulse. A small volume of material at the material surface can be evaporated (or ablated) if it is heated in a timescale like femtosecond laser pulse. The provided energy gradually allows the heat to be absorb into the bulk of the piece, never attaining a sufficiently high temperature at a particular point. Therefore, there is no thermal processing as in the case of ns pulses. Therefore, ultrashort (fs) pulsed lasers cause no heat impact and no thermal tension in the material, thereby inducing minimal changes on material chemical characteristics. Because fs laser induce minimum micro cracks, they also produce very smooth processed surfaces [34]. Finally, due to minimal heating phenomena, melting effects and surface damages are reduced. These characteristics allow ultrafast lasers to precisely control and manipulate the states of materials [31][35].

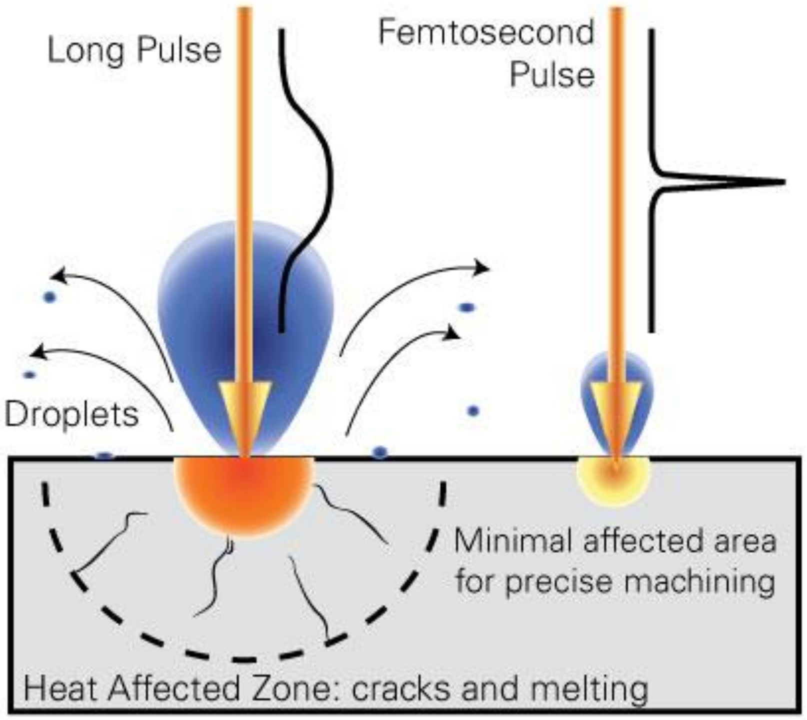

Figure 2.1.1-1: Long-pulse and ultrafast-pulse laser interaction with a target material. Long-pulse lasers reduce in a larger heat-affected zones and larger shock waves compared with ultrafast (fs) lasers, leading to minimum material damage.

Femtosecond laser ablation allows material removal from materials with minimal debris generation, high penetration and precision patterning. Since the pulse duration of a fs laser is shorter than the time constant of thermal diffusion, thermal effects into the surrounding material are minimized during the ablation process. fs pulsed laser interaction with matter triggers a variety of timescaledependent processes [36], summarized in **Figure 2.1.1-2** along with associated timescales that take place following the absorption of the laser pulse by the target material: 1) carrier excitation, 2) thermalization, 3) carrier removal, and 4) thermal and structural effects [35]. A threshold at about 10^{-12} - 10^{-11} s distinguishes the regimes between non-thermal and thermal processes. As illustrated in **Figure 2.1.1-2** for pulse duration τ_p significantly less than electron-to-lattice (ions) non-thermal pathways may be accessed that take place on a timescale shorter than a picosecond, hence before thermal processes are initiated. Laser irradiation is reported to cause changes to the local chemistry and local morphology. Nevertheless, there are still several aspects of fs laser induced modification of solids that need to be interpreted. For materials such as metals or semiconductors, thermal effects play a major role for material response. Pulse duration τ_p is an important parameter that affects such thermal effects. In these materials free carriers transfer energy to the lattice within a few ps, after which material melting and evaporation occur. By carefully choosing laser beam parameters (wavelength, pulse duration, fluence) for laser processing, it is possible to process materials, like metals, dielectric, semiconductors, biomaterials and solid materials, at high precision using more cost-efficient, longer-pulse, laser systems [36]. Upon photon absorption electrons are excited from their equilibrium states into higher-lying unoccupied states. The initial electronic excitation is followed by a complex hierarchy of secondary processes. The excited electrons relax and the deposited energy is redistributed through a number of processes which eventually end in the structural modification of the material [13]. The four regimes with different timescales that illustrated in figure and reported above are distinguished analytically [35].

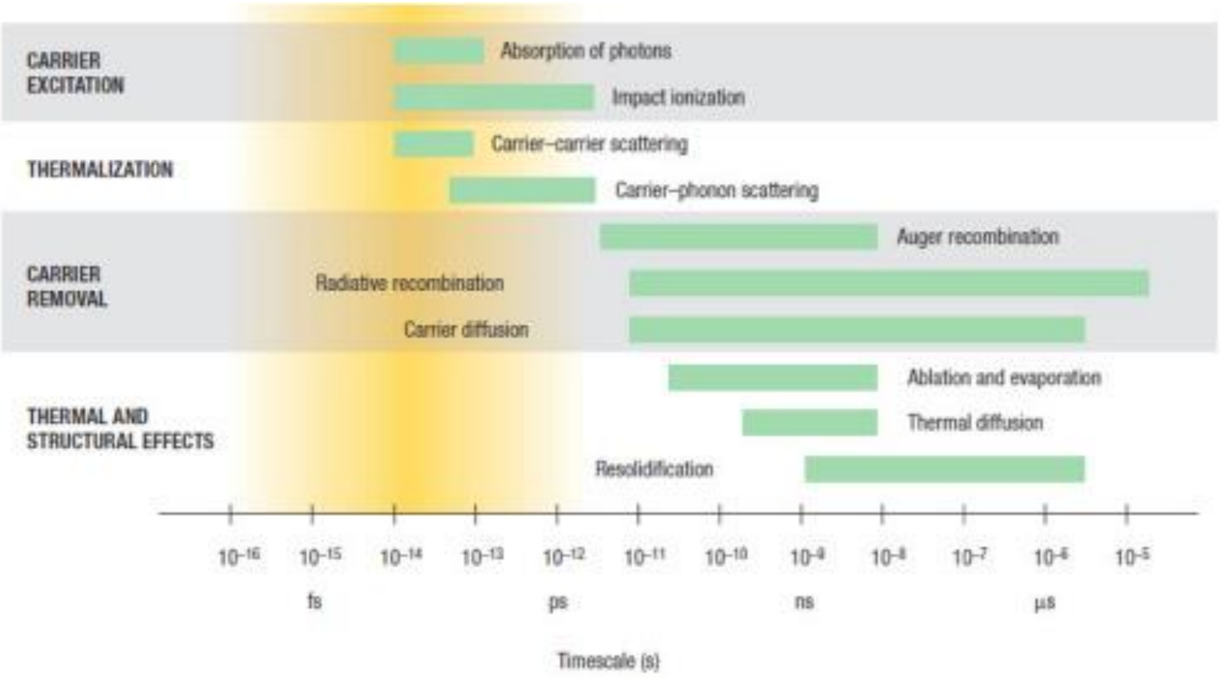

Figure 2.1.1-2: General schematics of excitation/relaxation processes in an insulator. Timescales of various electron and lattice regimes following ultrafast laser semiconductor interaction. Each green bar represents an approximate range of characteristic times over a range of carrier densities from 10^{17} to 10^{22} cm^{-3} [35].

Carrier excitation is the movement of an electron to a higher energy state due to absorption of photons by a laser beam. When the photon energy is larger than the bandgap, single photon absorption is the dominant mechanism for exciting valence electrons to the conduction band. Free carrier absorption increases the energy of carriers in the electron–hole plasma or that of the initially free electrons in a metal, although it does not alter its number density. Multiphoton absorption is important if the direct gap is greater than the photon energy, especially in transparent insulators, or if single-photon absorption is inhibited by band filling. In solids, scattering causes rapid dephasing of the coherence between the excitation and the electromagnetic field that causes it. If some of the carriers are exited well above the band gap (or Fermi level in metals), impact ionization can generate additional excited states.

Thermalization: After excitation, electrons and holes are redistributed throughout the conduction and valence bands by carrier–carrier and carrier–phonon scattering. Carrier–carrier scattering can cause dephasing in less than 10 fs, but it takes 100s fs for the carrier distribution to approach a Fermi–Dirac distribution. In a carrier–phonon scattering process, free carriers lose or gain energy and momentum by emission or absorption of a phonon. Although carrier–phonon scattering does not change the number of carriers, their energy decreases due to spontaneous phonon emission, which transfers energy to the lattice. In metals and semiconductors, carrier–carrier and carrier–phonon scattering occur concurrently during the first few hundred femtoseconds after excitation. Because the emitted phonons carry little energy, it takes many scattering processes, and therefore several picoseconds, before the carriers and the lattice reach thermal equilibrium.

Carrier removal: Once the carriers and the lattice are in equilibrium, the material is at a well-defined temperature. Although the carrier distribution has the same temperature as the lattice, there is an excess of free carriers compared to that in the thermal equilibrium. The excess carriers are removed either by recombination of electrons and holes or by diffusion out of the excitation region. In semiconductors, carrier confinement due to a decrease in bandgap on the excitation of a high carrier density, slows down the diffusion away from the photo-excited region. This laser induced bandgap renormalization has been confirmed by theory as well as by experimental results.

Thermal and structural effects. Material excited by ultrashort laser pulses can achieve the equilibrium temperature in just a few picoseconds, but the removal of excess carriers takes longer. On the time scale of 10^{-11} sec and below carriers and lattice come to an equilibrium temperature and heat is diffused from the material surface to the bulk. If the lattice temperature exceeds the melting or boiling point, melting or vaporization can occur, but not on the ps timescale. The material is superheated but remains solid until regions of liquid or gas nucleate. Starting from nucleation sites at the surface, the liquid and/or gas phase expands into the material. As the energy deposited by the laser pulse is converted to kinetic energy of the lattice ions, individual atoms, ions, molecules or clusters can leave the surface, leading to ablation. Thermal diffusion limits expansion of the liquid region by cooling the photo-excited region. If no phase transition occurs, the temperature reverts back to the ambient value on the timescale of microseconds. If melting or vaporization has occurred, then re-solidification or condensation ensues as the temperature falls below the melting or boiling points, respectively; however, the material does not necessarily revert back to its original structure or phase.

Mechanisms leading to structural modifications using exposure to ultrashort (fs) pulses are no thermal and leads to a different type of modification. Laser ablation techniques have been used for selective material removal to create precise patterning on several materials. Ablation processing utilizes large pulse energies to cause boiling at the melt surface. The resulting superheating of the liquid phase and high nucleation rates of the gas phase cause material ejection from the surface. Thus, ablation can take place only if a laser beam is absorbed by the material to be ablated. The onset of ablation occurs above a threshold fluence I_{th}, which depends on the absorption mechanism, material properties (e.g. microstructure, morphology and the presence of defects) and laser parameters (wavelength, pulse duration) [37]. Ablation processing by laser pulses, utilizes high pulse energies to cause boiling at the melt surface, therefore ablation can take place only if a laser beam is absorbed by the material to be ablated, leading to cumulative changes in the surface texture, morphology, and chemistry. For instance, residual heat left after material ablation can lead to further melting or other thermally activated processes in the surrounding material volume [38], which can result in complex multi-scale material modifications that can be utilized by various laser material processing applications. Mechanisms leading to structural modifications using ultrashort (fs) pulses are not thermal and lead to a different type of modification with minimal material damage. In the case of fs pulsed lases, the plasma recombines before thermal diffusion, shock wave propagation, and cavitation set in. Ablation of the substrate is confined, at least initially, to a small volume. Although the intensity required to initiate breakdown is fairly high, the short duration of the pulse allows the threshold intensity to be achieved with a lower intensity. The combination of localized excitation and low threshold fluence can greatly reduce the extent of damage to surrounding areas, so that the size of the affected material can be microscopic, very close to the diffraction-limited focusing volume. As a consequence, structures fabricated using fs laser ablation techniques provide excellent control over micro- and submicron scales [39].

2.1.2. Pulsed laser ablation of biological tissues

Although there is extensive knowledge on laser processing of solid materials and metals, much less is known about ablation of biomaterials, despite the fact that mechanisms of pulsed laser ablation interaction with biological tissues were reported soon after the invention of the pulsed ruby laser by Maiman in 1960 [40]. The first clinical application of pulsed laser ablation was reported in the early 1970s [40]. Researchers investigate the mechanisms of pulsed laser tissue ablation since.

The mechanical properties of biological tissues are of great importance to laser ablation, as both tissues elasticity and strength modulate the kinetics and dynamics of the ablation process. When a laser beam propagates through matter, ballistic beam intensity diminishes due to two processes: absorption and scattering. The spatial distribution of energy density of laser irradiation drives the ablation process. The optical properties of the tissue to be ablated, mainly its scattering and absorption properties, determine the energy distribution of the propagating laser beam, which drives the ablation process. Such optical properties depend on tissue composition and morphology.

Beginning with absorption, it seems that there are two types of multi-photon absorption: simultaneous and sequential. In simultaneous absorption, there is no real intermediate energy state i.e., the material is transparent at that wavelength. Instead, there is a virtual intermediate energy state and two-photon absorption happens only if another photon arrives within the virtual state lifetime. For this to occur high intensities are required, which can be provided by a tightly focused ultrafast laser beam. In sequential multi-photon absorption, the absorbing species are excited to a real intermediate state, where, a second photon is absorbed. The presence of the intermediate energy state implies that the material is absorbing at this specific wavelength. The optical absorption properties of a tissue sample can be characterized by its absorption coefficient μ_α (cm^{-1}) defined by Beer-Lambert's law as:

$$T = \frac{I}{I_0} = e^{-\mu_a x}$$

Equation 2.1.2-1

Where T is optical transmission and x is optical path depth.

Regarding tissue scattering, it seems that optical scattering arises from refractive index spatial variations within the tissue, which dependents on the composition, size, and morphology of cellular and extracellular matrix tissue components [40]. When scattering is negligible or absent, the optical penetration depth, δ, of the incident radiation can change and the absorption coefficient defines the characteristic depth to which the tissue is heated. However, wavelength and laser beam diameter can influence optical properties and at wavelengths where optical scattering is significant and optical penetration depth is smaller than $1/\mu_\alpha$.

2.1.3. Propagation of Light inside Porous Scaffolds

2.1.3.1. Gaussian Beam

Electric field of Gaussian wave propagates in z direction. The beam power is located within a finite distance from the beam axis. Intensity distribution in the transverse plane follows Gaussian distribution.

$$\mathrm{I} = \mathrm{I}_0 \left(\frac{\mathrm{w}_0}{\mathrm{w(z)}}\right)^2 \mathrm{e}^{-2\left(\frac{\mathrm{r}}{\mathrm{w(s)}}\right)^2}$$

Equation 2.1.3.1-1

$$w(z) = w_0 \sqrt{1 + \left(\frac{z}{z_R}\right)^2}$$

Equation 2.1.3.1-2

Where w_0 is the beam waist at the focal plane (z=0) and w(z) is the beam radius at any transverse plane located at z. **Figure 2.1.3.1-1** shows notation for the lowest order Gaussian beam diverging away from its waist. Within any transverse plane the beam intensity peaks on the beam axis and drops by the factor $1/e^2 \approx 0.135$ at the radial distance r = w(z), which is called the beam radius. w(z) is minimum at the beam waist (z = 0) where $w(0) = w_0$. The beam diameter 2w is called the spot size of the Gaussian beam. The beam radius and spot size monotonically increase with increasing distance from the beam waist.

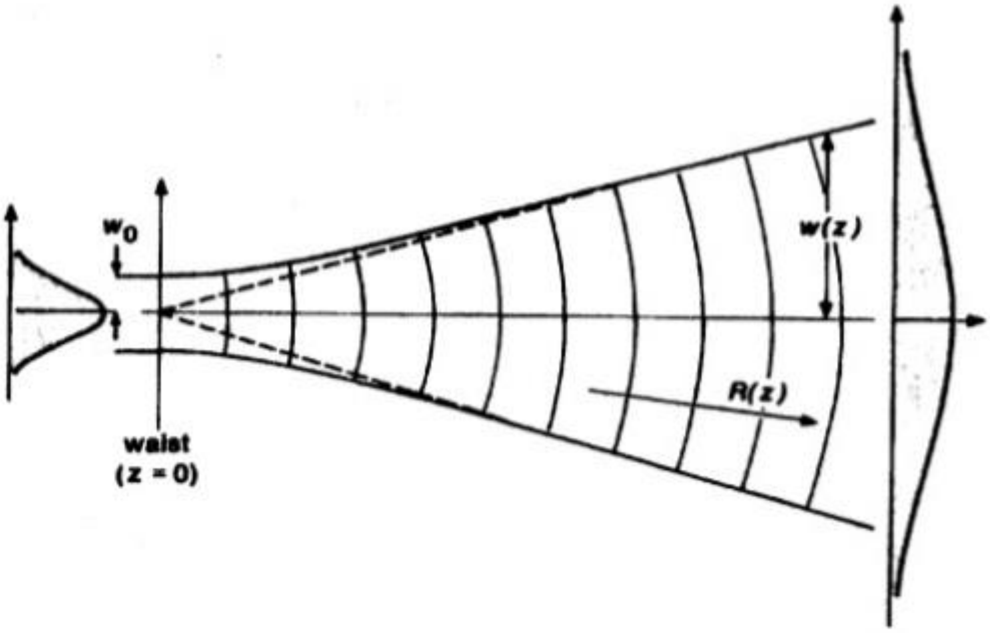

Figure 2.1.3.1-1 : The beam radius and spot size monotonically increase with increasing distance from the beam waist.

The paraxial approximation assumes that the plane wave is modulated by a complex amplitude that is a slowly varying function of position. **Figure 2.1.3.1-2** shows the fractional power transfer for a Gaussian beam of radius w passing through a circular aperture of diameter 2a. The effective diameter d_{th} and area A_{th} of a uniform cylindrical beam (top hat beam) with the same peak intensity and total power as a cylindrical Gaussian beam equals $d_{th} = \sqrt{2w}$ and $A_{th} = \frac{\pi w^2}{2}$. An aperture with radius a=w will transmit ≈86% of the total beam power. An aperture of diameter $\pi \cdot w$ transmits ≈ 99% of the total beam power. The diffraction effects on an ideal Gaussian beam of a sharp edge circular aperture of diameter $\pi \cdot w$ will cause near field diffraction ripples with intensity variation ΔI/I =17% in the near field, along with a peak intensity reduction of 17% on axis in the far field.

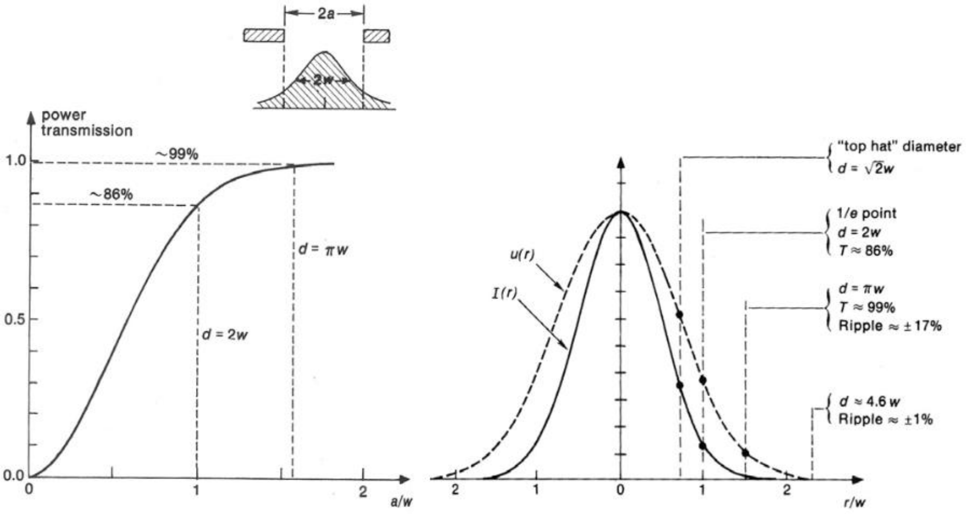

Figure 2.1.3.1-2 : Distance at which 1/e times amplitude on the axis. Aperture transmission – diffraction effects. The fractional power transfer for a Gaussian beam of radius w passing through a circular aperture of diameter 2a

All Gaussian beam parameters can be related to the waist spot size w_0, w_z and the z_R by:

$$w_0 = \sqrt{\frac{\lambda z_R}{\pi}} \quad , \qquad w_z = w_0\sqrt{1+\left(\frac{z}{z_r}\right)^2} \quad , \qquad z_r = \frac{\pi {w_0}^2}{\lambda}$$

Equation 2.1.3.1-3

And the radius of curvature by:

$$R_z = Z + \frac{{Z_R}^2}{Z}$$

Equation 2.1.3.1-4

Where parameter w_0 or z_R at the beam waist is in the relative of the wavelength λ in the medium. The intensity of a Gaussian beam falls off very rapidly with radius beyond the spot size w. The total Power in an optical beam is given by:

$$P = \iint |u|^2 \, dA$$

Equation 2.1.3.1-5

Over the cross sectional area. Now the radial intensity variation of a Gaussian beam with spot size w can be inferred as:

$$I(r) = \frac{2P\, e^{-2{\frac{r}{{w_z}^{2}}}^{2}}}{\pi {w_z}^{2}}$$

Equation 2.1.3.1-6

2.1.3.2. Beam divergence

In certain distance z_R away from the focal plane, the laser beams follow plane wave characteristics. But after that, laser beam width diverges from being nearly linear. The corresponding angle of deviation of beam width equals $\theta = \frac{\lambda}{\pi w_0}$

The distance which the beam travels from the waist before the beam diameter increases by $\sqrt{2}$ or before the beam area doubles equals $z_R = \frac{\pi {w_0}^{2}}{\lambda}$ (Rayleigh range), see **Figure 2.1.3.1-3**. Since the beam has its minimum width at z=0, it achieves its best focus at the plane z=0. In either direction, the beam gradually grows out of focus.

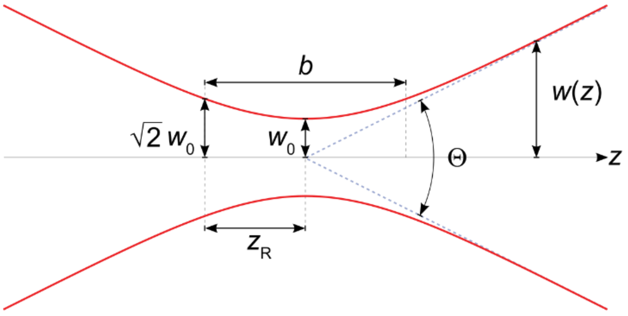

Figure 2.1.3.1-3: the depth of focus of a Gaussian beam as a function of the distance z. W_0 is the beam waist, b is the depth of focus, Z_R the Rayleigh range and θ the total angular spread

If a Gaussian beam is focused down to a waist and then expands again, the full distance between the 2 w_0 beam radii, within which the beam can be considered as nearly collimated, the depth of focus, is called “the confocal parameter of the Gaussian beam” and equals $b = 2z_R = \frac{2\pi {w_0}^2}{\lambda}$.

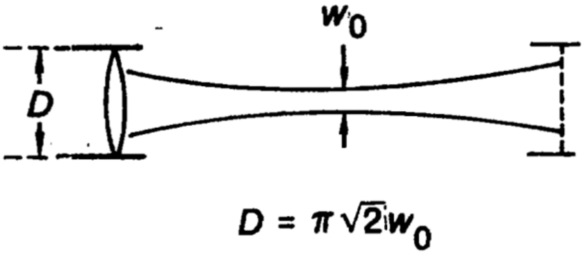

Figure 2.1.3.1-4 : The beam focusing slightly to a waist with spot size w0 at one Rayleigh range out and then re-expands to the same diameter D two Rayleigh ranges out

The beam focusing slightly to a waist with spot size w_0 at one Rayleigh range out and then re-expands to the same diameter D two Rayleigh ranges out as $D = \pi\sqrt{2}\, w_0$

Relation between the collimated beam distance and the transmitting aperture size using this criterion is then described by Collimated range:

$$collimated\ range = 2z_R = \frac{2\pi {w_0}^2}{\lambda} = \frac{D^2}{\pi\lambda^2}$$

Equation 2.1.3.1-7

Beam size expands linearly with distance. The 1/e spot size w(z)for the field amplitude in the field far for a Gaussian beam coming from a waist with spot size w_0 by:

$$w(z) = \frac{w_0 z}{w_R} = \frac{\lambda z}{\pi w_0}$$

Equation 2.1.3.1-8

The on-axis beam intensity in the far field is given by:

$$I_{axis}(z) = \frac{2P}{\pi w^2(z)} = \frac{P}{\frac{\lambda^2 z^2}{2\pi {w_0}^2}}$$

Equation 2.1.3.1-9

The solid angle for an equivalent top hat angular distribution in the far field call $\Omega_{th}(z)$, is thus given by:

$$\Omega_{th} = \frac{\pi w^2(z)}{2z^2} = \frac{\lambda^2}{2\pi {w_0}^2}$$

Equation 2.1.3.1-10

2.1.4. Analytic Models for Ablation

According the theoretical background of Principles of laser, a model was design to describe the laser Ablation when the laser beam focus inside Porous Collagen Scaffolds. After these approaches the theoretical and the experimental part have to be in agreement.

Assuming that ablation is equal or bigger than w_r of a Gaussian beam when the laser beam is focusing inside a scaffold. That means ablation takes place inside a volume where $I>I_{th}$. This idea can be described in figure below [**Figure 2.1.4-1**].

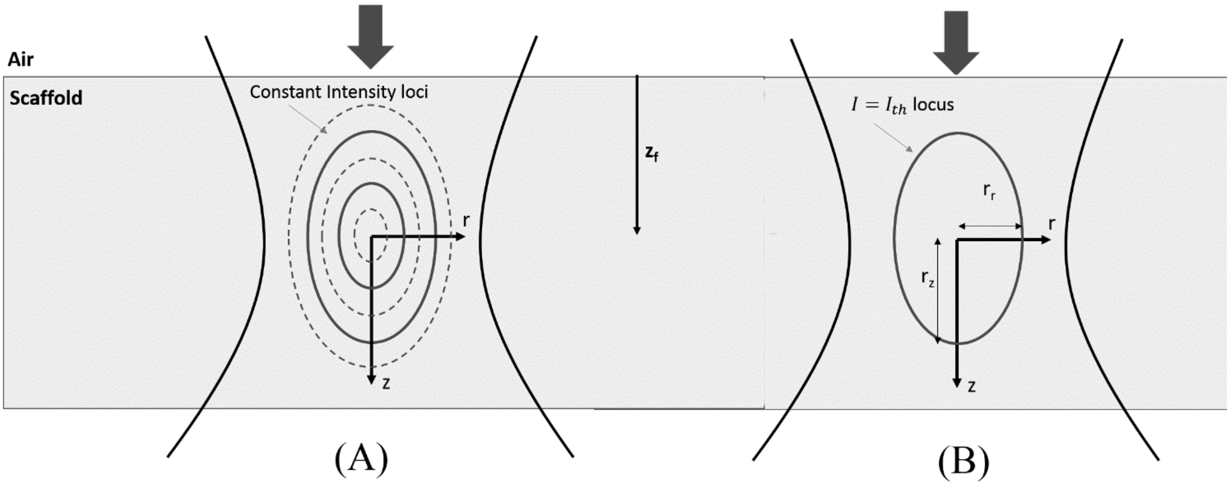

Figure 2.1.4-1 : Propagation of a Focusing Gaussian Beam inside a Scaffold. (A) The constant intensity locus when a laser beam focusing inside a material. (B) The ablation volume which can be described by radial and axonal radius.

The radius in the radial direction r_r and the radial in the axial direction r_z, define the locus of constant intensity I where the ablation take place. Model this according the Gaussian theory and find this locus, an equation of radius resulting depending on the Numerical Aperture (NA) of the focusing lens and the ratio b of Intensity. The intensity profile a Gaussian beam propagating inside a medium without absorption or scattering around the focus ($r = z = 0$) is:

$$\mathrm{I} = \mathrm{I}_0 \left(\frac{\mathrm{w}_0}{\mathrm{w(z)}}\right)^2 \mathrm{e}^{-2\left(\frac{\mathrm{r}}{\mathrm{w(w)}}\right)^2}$$

Equation 2.1.4-1

So the locus $r(z)$ of constant intensity I equals:

$$r_r^{*2} = \frac{1}{2}(1 + (\mathrm{NA} \cdot \mathrm{z}^*)^2) \cdot \ln(\frac{\mathrm{b}}{1 + (\mathrm{NA} \cdot \mathrm{z}^*)^2})$$

Equation 2.1.4-2

Where

$$\mathrm{b} = \frac{\mathrm{I}_0}{\mathrm{I}} = \frac{2 \cdot \mathrm{P} \cdot \pi \cdot (\mathrm{NA})^2}{\lambda^2 \cdot \mathrm{I}}$$

Equation 2.1.4-3

And r_r^*, r_z^* are non-dimensionalized coordinates:

$$r_r^* = \frac{r}{\mathrm{w}_0}$$

$$r_z^* = \frac{z}{\mathrm{w}_0}$$

Equation 2.1.4-4

Assuming ablation takes place when

$$I \geq I_{th}$$

Equation 2.1.4-5

Boundary of the ablated volume is approximated by the locus $r_r^*(r_z^*, NA, b(I_{th}))$:

$$r_r{}^{*2} = \frac{1}{2}(1 + (NA \cdot r_z{}^{*})^2) \cdot ln(\frac{b(I_{th})}{1 + (NA \cdot z^{*})^2})$$

Equation 2.1.4-6

where

$$b(I_{th}) = \frac{2 \cdot \pi \cdot \mathrm{P} \cdot (\mathrm{NA})^2}{\lambda^2 \cdot I_{th}}$$

Equation 2.1.4-7

After calculations above, ablation radius in the radial direction r_r is defined as $\mathrm{r}^{*}(z^{*} = 0)$ and is given:

$$r_r^{*} = \sqrt{\frac{1}{2} \cdot ln(b(I_{th}))}$$

$$r_r = \frac{\lambda}{\pi NA}\sqrt{\frac{1}{2} ln\left(\frac{2\pi \cdot \mathrm{P} \cdot (NA)^2}{\lambda^2 I_{th}}\right)}$$

Equation 2.1.4-8

The same with the ablation radius in the axial direction r_z is defined as $\mathrm{z}^{*}(r^{*} = 0)$:

$$r_z{}^{*} = \frac{\sqrt{b(I_{th}) - 1}}{NA}$$

$$r_z = w_0 \frac{\sqrt{b(I_{th}) - 1}}{NA} = \frac{\lambda}{\pi \cdot NA^2}\sqrt{\frac{2\pi \cdot \mathrm{P} \cdot (\mathrm{NA})^2}{\lambda^2 \cdot I_{th}} - 1}$$

Equation 2.1.4-9

2.2. Analytic Study of Laser Ablation

2.2.1. Light Intensity Profile

According to the literature of laser ablation, the basic characteristic is ablation held on the top of the surface. When material is solid then the ablation is superficial due to absorption and scattering phenomena in solid materials. In the case of PCS ablation by a pulsed laser beam, ablation happens in a material with very low average mass density. A laser beam can be focused both inside a PCS as well as on its surface. Inside a PCS, scattering and absorption phenomena play a main role in laser ablation characteristics. To first approximation, absorption and scattering phenomena are neglected and the Gaussian beam model is utilized to describe the intensity of light when a laser beam is focused inside a PCS. Therefore, according theory of laser beam intensity, characterization of Laser-Induced Ablation of Porous Collagen Scaffolds can calculate the radius of laser beam. Radius of ablation were evaluated according to the intensity of laser depending from w_z, w_0 and the ration of intensity (I) and $I_{(th)}$. The values of w_z and w_0 replaced on the **Equation 2.2.1-1**. A non-dimensional values of radius and waist of laser w_0, represented in terms of α and b.

- $I = I_0 \left(\frac{W_0}{W_Z}\right)^2 e^{-2\left(\frac{r}{W_Z}\right)^2} \rightarrow \mathrm{r} = \mathrm{W_z}\sqrt{\ln\frac{\mathrm{W_0}}{\mathrm{W_Z}}\sqrt{\frac{\mathrm{I_0}}{\mathrm{I}}}}$ (1)

Equation 2.2.1-1

- $Z_R = \frac{\pi {W_0}^2}{\lambda}$

Equation 2.2.1-2

- $W_Z = W_0\sqrt{1+\frac{Z^2}{{Z_R}^2}} \rightarrow W_Z = W_0\sqrt{1+\left(\frac{Z\lambda}{\pi {W_0}^2}\right)^2}$ (2)

Equation 2.2.1-3

- $\frac{r}{W_0} = \sqrt{(1+a^2)\, ln\frac{1}{\sqrt{1+a^2}}\sqrt{b}}$ (3)

Equation 2.2.1-4

Where:

- $a = \frac{Z\lambda}{\pi {W_0}^2}$
- $b = \sqrt{\frac{I_0}{I}}$ ratio of intensities

Equation 2.2.1-5

In order to estimate what happening when z and r is zero respectively, the **Equation 2.1.3.1-4** solved. First the value α set as zero and the non-dimensional r/w$_0$ estimated and shows that is depended on value b. When a non-dimensional values of radius (r) and waist of laser (w$_0$) is zero then α is depended on b value.

- ❖ If: a=0 →

$$\frac{r}{W_0} = \sqrt{(1+a^2)\ln\frac{1}{\sqrt{1+a^2}}\sqrt{b}} \rightarrow \frac{r}{W_0} = \sqrt{\ln\sqrt{b}}$$

$$\frac{r}{W_0} = \sqrt{\ln\sqrt{b}} \rightarrow b = e^{2\left(\frac{r}{W_0}\right)^2}$$

Equation 2.2.1-6

- ❖ If: $\frac{r}{W_0}$=0 →

$$\frac{r}{W_0} = \sqrt{(1+a^2)\ln\frac{1}{1+a^2}\sqrt{b}} \rightarrow 0 = \sqrt{(1+a^2)\ln\frac{1}{1+a^2}\sqrt{b}}$$

$$a = \sqrt{\left(\sqrt{b}-1\right)}$$

$$b = (1+a^2)^2$$

Equation 2.2.1-7

2.2.2. Ablation Volume Estimation

Here, it is assumed that ablation takes place within the volume where light intensity exceeds the intensity threshold I_{th}, a characteristic of the ablated material. **Figure 2.2.2-1** reveals that radius of ablation r_z in the axial (along with the laser direction) direction and the radial direction r_r are effective by intensity in different ways. The axial resolution r_z depends strongly on both optical and intensity of light as well. As laser intensity increases, the volume that is removed grows. The NA of the focusing lens affects strongly axial radius r_z. On the other hand, the radial radius of the ablation volume does not depend so significantly on focusing lens NA or laser intensity. NA has less effect on r_r^* than $r_z{}^*$. When $b(I_{th}) = \frac{I_0}{I_{th}}$ becomes less or equal to 1, no ablation is observed. When $1 \leq b(I_{th}) < 10$ then $r_r < w_0$. When $b(I_{th}) \geq 10$ then $r_r \geq w_0$. **Figure 2.2.2-1** shows the non-dimensional values of axial and radial resolution relation on respectively values of NA according the equations:

$$r_z{}^* = \frac{r_z}{\mathrm{w}_0}, \qquad r_r{}^* = \frac{r_r}{\mathrm{w}_0}$$

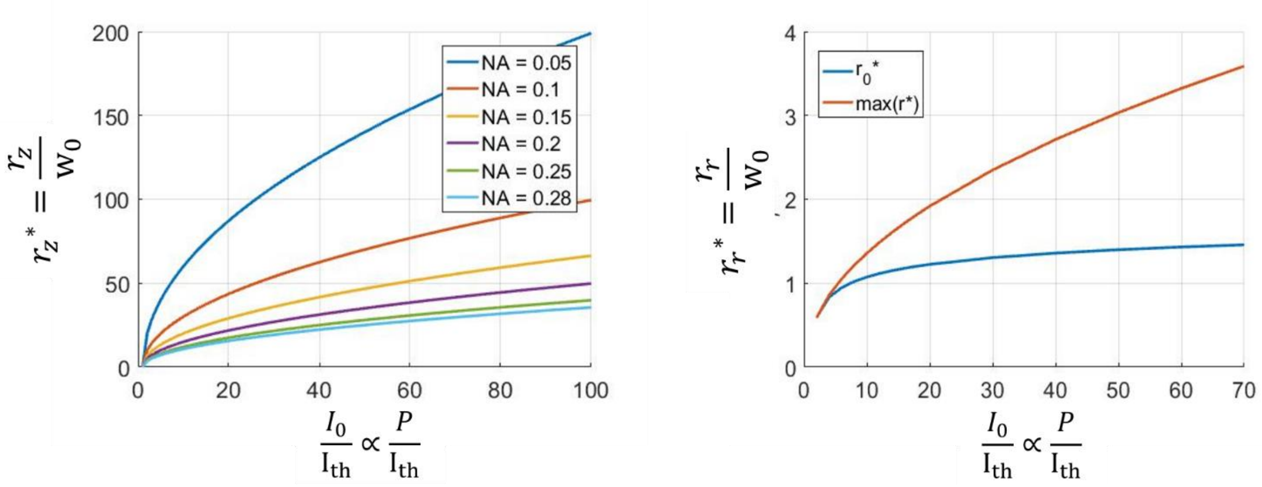

Figure 2.2.2-1: Effect of NA, P on Axial Resolution $\boldsymbol{r_z}^*$ and Radial Resolution $\boldsymbol{r}_{\mathrm{r}}{}^*$

Ablation locus as function of ($\mathrm{I_{th}}$) showing in the graph below **Figure 2.2.2-2** where in generally r_r^* is bounded and $r_r{}^* < r_z{}^*$. **Figure 2.2.2-2**.

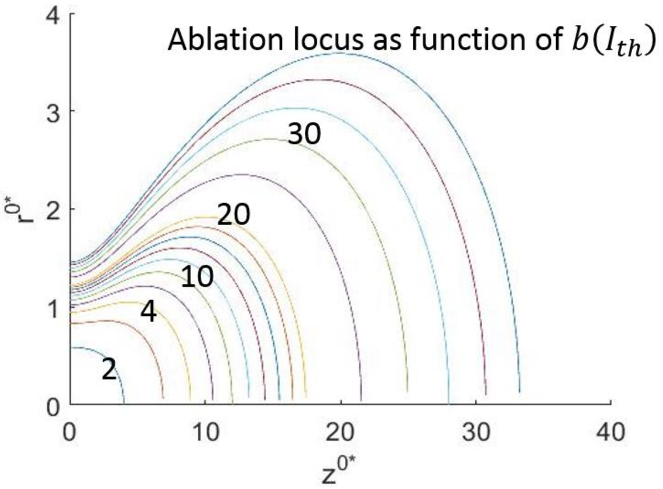

Figure 2.2.2-2: Radial radius of laser beam and axial radius relationship. Ablation locus as function of b(I_{th}) can be estimate.

2.3. Experimental Methods

In this project, two kinds of PCS were used. First, "thin" PCS of ≈20 μm mean pore diameter and 150 μm thickness, fabricated in devices. Second, "thick" PCS of ≈100 μm mean pore diameter and 2-3mm thickness **Figure 2.3-1**. Samples were laser ablated by a focused fs laser beam in order to estimate intensity threshold I_{th} and measure axial and radial resolution r_z and r_r respectively.

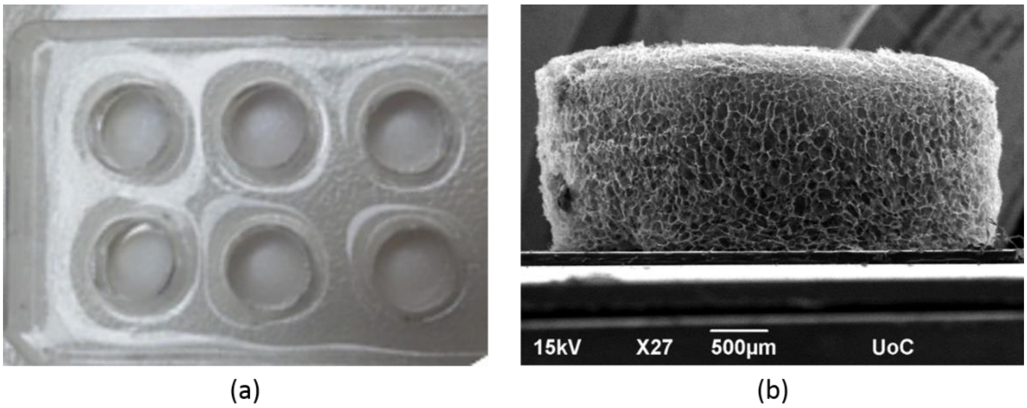

(a) (b)

Figure 2.3-1: Porous collagen scaffolds utilized in this study. (a) "Thin" PCS fabricated inside a device. (b) Scanning Electron Microscopy of a "thick" PCS.

2.3.1. PCS Fabrication

Both thin and thick PCS were fabricated by lyophilization as described in [41]. Overall, PCS fabrication consists of four major processes:

- Preparation of collagen suspension: Microfibrillar collagen I fibers and other components (in this study glycosaminoglycans (GAG) or fibronectin isoforms) are dissolved in 0.05M acetic acid. The resulting suspension contains collagen particles and air bubbles.
- Freeze-drying: The collagen suspension is poured into a mold that provides the shape of the final dry scaffold. Lyophilization is a dehydration method in which the icy water contained in the material passes directly from the solid phase to the gases as shows in the figure [Figure 2.3.1 1]. Thin PCS were placed inside a PDMS scaffold, analogue of well-plates, on a glass surface [Figure 2.2.2 1] and microfabricated in this device. The aqueous part is removed by first freezing the suspension, and then removing the resulting ice crystals via sublimation. What remains is a dry porous scaffolds-like material whose struts contain the solid material (collagen, GAG, ECM proteins) that was trapped between ice crystals during freezing. The outcome of the freeze-drying process is a dry scaffold sheet. On the other hand, cell scaffold interaction experiments or biomaterial characterization experiments need much smaller cylindrical samples of scaffolds. These samples are cut from the original sheet using biopsy punches (Miltex).
- Scaffold Cross-linking: Formation of additional intra-molecular bonds in the scaffold in order to improve resistance to proteinase degradation and increased the material stiffness. Cross-linking can be implemented by thermal (dehydro-thermal treatment) or chemical (chemical cross-linkers) means.
- Sample preparation: *In vivo* applications of collagen scaffolds in skin and peripheral nerve regeneration require scaffolds of relative large dimensions (on the order of cm), and planar or tubular geometry respectively. In contrast in vitro applications of scaffolds for studying cell-scaffold interactions require multiple copies of small samples (size around 5-8mm), which are prepared by cutting scaffold sheets.

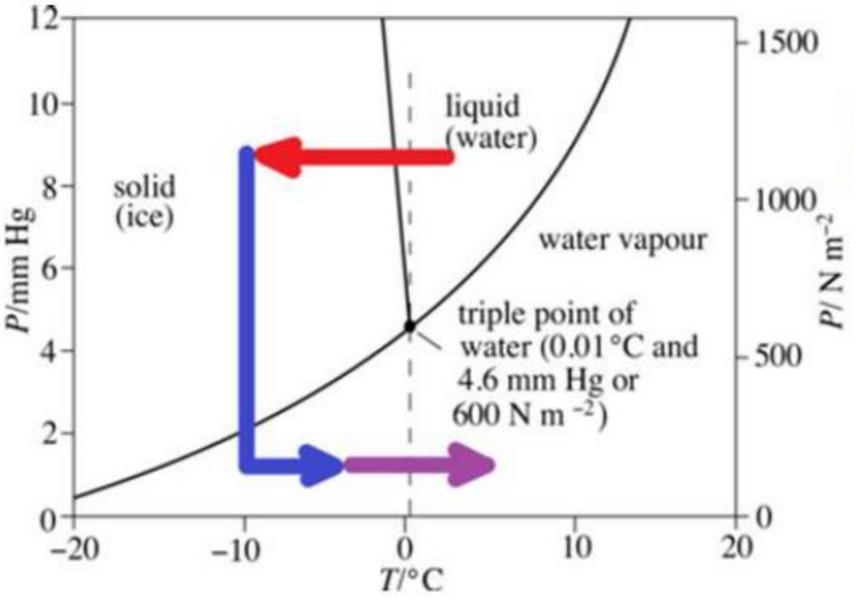

Figure 2.3.1-1: Three Stages of lyophilization. Red color shows the freezing stage. Blue shows the Primary Drying and Purple the Secondary Drying stage.

2.3.2. Ablation Setup

All experiments tool place in the optical setup shown in **Figure 2.3.2-1**, which is located at the ultrafast micro and nano processing lab at FORTH-IESL.

A Pharos laser system (Light Conversion Ltd, Vilnius, Lithuania) had been used for PCS laser microfabrication. Pharos is a compact solid state laser with ytterbium doped with potassium, gadolinium and tungsten (Yb:KGW) active medium. It emits at a central wavelength of 1026 nm and supports harmonic generation of the fundamental at 513nm. It's a single unit integrated fs laser system combining millijoule pulse energies and high average power with maximum pulse energy E_p= 1.5 mJ and repetition rate f_p ranging from 1 kHz up to 200 kHz. The pulse width τ_p can vary from 170 fs to 10ps. For PCS microfabrication experiments τ_p =170 fs and f_p =1 kHz and λ= 1026 nm.

The laser beam provided by the Pharos laser is guided by high-reflective dielectric mirrors and is focused into the sample through a 10x objective lens (Mitutoyo 10x Plan Apo Infinity Corrected Long WD Objective, 0.28NA, focal length f =200 mm). The focus point was observed by a CCD camera connected to a PC. PCS samples where positioned on a XYZ motorized stage (Standa) controlled by a high-precision motion controller. Collagen samples were placed so that their top surface was approximately perpendicular to the incident laser beam. Laser irradiation was performed in air environment. Laser irradiation was blocked or enabled by a shutter, depending on experimental process. The average laser beam power was modified via a filter. Laser power measured by a Power meter after filter and before the sample. The system is controlled by a custom GUI written in Labview by Andreas Lemonis (ultrafast micro and nano processing lab, FORTH-IESL).

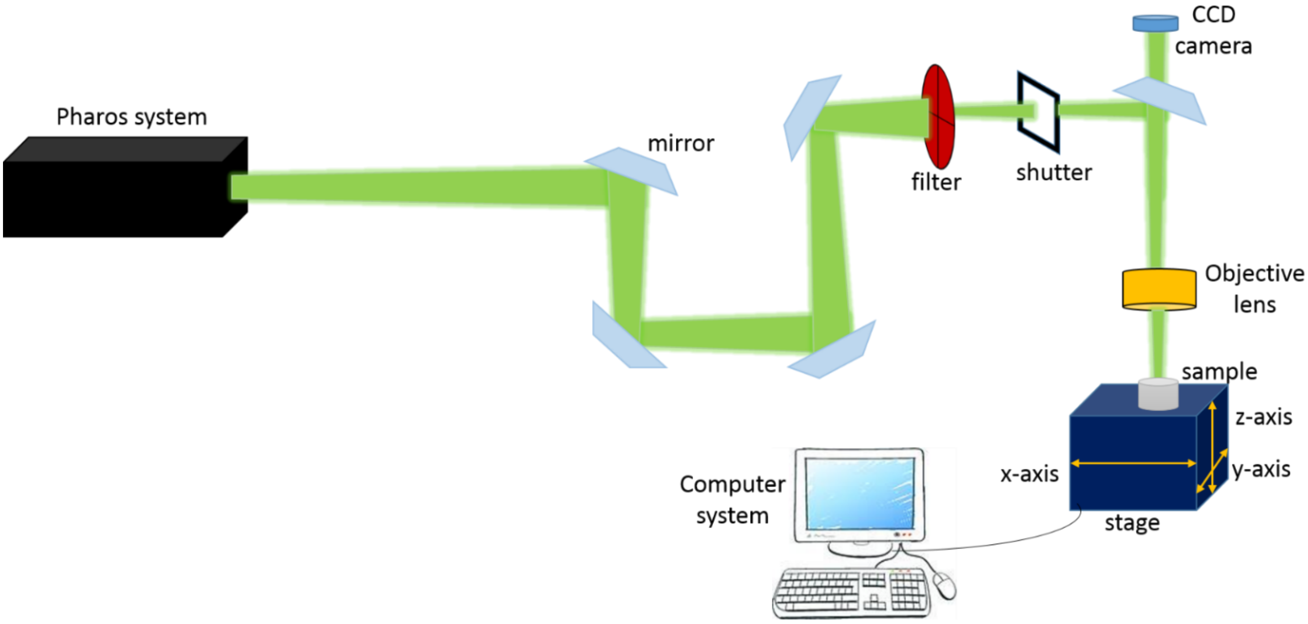

Figure 2.3.2-1: Experimental set up. Laser beam propagate from a Pharos laser system through high reflective dielectric mirrors. A filter controls the laser power and a shutter can manually let the laser beam go over and start the irradiation process. After, the beam focus through an objective lens. The focus observe by a CCD camera, united with a computer system. Samples position and stabilized perpendicular to the incident laser beam on a high-precision X– Y –Z translation stage, united also with the computer system through a proper software.

2.3.3. Ablation Characterization Experiments

Two types of porous collagen have been used [2.3]. Characterization of a material's surface properties is needed, in order to relate important surface characteristics to biological responses [4.1.1]. Topographic properties may all influence the way cells interact with a material. Thin collagen and thick, were characterized with simply stereoscope microscopy and Scanning Electron Microscopy respectively for their surface and topology properties.

2.3.3.1. Scaffold microfabrication

Samples were stabilized on the top surface of the XYZ stage by two ways. First, both thin and thick PCS, were stuck using double-sided tape (Melca Double Sided Tape) on a Plain Glass Microscope Slides. Glass placed using double-side tape on the top of the surface. This stabilized the samples during the movement. Second, cylindrical thick PCS samples (~2mm width and ~3mm diameter) were stabilized inside the top part of a 200 µl pipette tip (Pipette tip, 200 µl, Biosphere® plus). The top of the pipette tip was cut and then position on the top of Plain Glass Microscope Slides and then on the surface of the XYZ stage via double-sided tape.

Then, the laser beam was focused on the top of PCS surface manually using a CCD camera that provides the GUI with a high-magnification image of the laser beam focusing location. The user selects a position on the surface as the "starting point" of the fabrication process via the ''set reference'' button on the GUI. Then, the user selects stage velocity. As soon as the user clicks the "start" button, the irradiation begins from the starting point according to the parameters chosen. **Figure 2.3.3.1-1**shows representative examples of ablation patterns into a thin PCS.

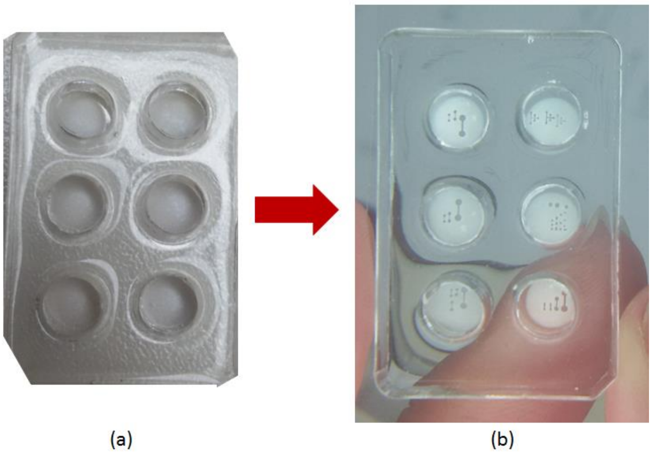

Figure 2.3.3.1-1: Device of thin PCS. (a) Before laser microfabrication and (b) After laser microfabrication.

2.3.3.1.1. Thin PCS: Estimation of Intensity Threshold

In order to estimate the intensity threshold I_{th} that can induce PCS ablation at 1026 nm, various simple patterns were ablated in thin PCS. Thin PCS were chosen due to their smaller pore size ($\approx$ 20 μm) that makes easier to detect ablation of tiny features. Standard ablation parameters utilized in these experiments were U = 2mm/s, Y-step = 10 μm. The main experimental variable of this experiment was laser power P, which varied between 1 to 5 mW. A 2D sketch program was utilized to generate a simple pattern (size 1mm x 0,5mm), consisting of lines and circles, to be ablated at various power levels.

2.3.3.1.2. Thick PCS: Characterization of Ablation Volume Size

Thick PCS were stabilized on the top surface of the XYZ stage by two ways. Fist, samples were stuck using double-sided tape (Melca Double Sided Tape) on a Plain Glass Microscope Slides. Glass placed using double-side tape on the top of the surface. This stabilized the samples during the movement. Second, cylindrical thick PCS samples (~2mm width and ~3mm diameter) were stabilized inside the top part of a 200 μl pipette tip (Pipette tip, 200 μl, Biosphere® plus). The top of the pipette tip was cut and then position on the top of Plain Glass Microscope Slides and then on the surface of the XYZ stage via double-sided tape.

The top surface of PCS samples was not flat and practically could not be set perfectly perpendicular to the laser propagation axis. In order to minimize experimental variability, PCS samples were initially flatten via a laser beam of $P = 40$ mW power using high stage velocity ($U = 10$ mm/s), manually focused on the middle of the PCS sample using the procedure described [**2.3.2]**. After flattening the top PCS surface, the laser beam went back to the initial point. The plane that corresponds to the laser focus during flattening was defined as z=0μm. **Figure 2.3.3.1-2** shows SEM images before and after PCS flattening. The utilized flattening process provided consistent results. Experimental results proved that flattening is absolutely necessary for repeatable precision laser ablation.

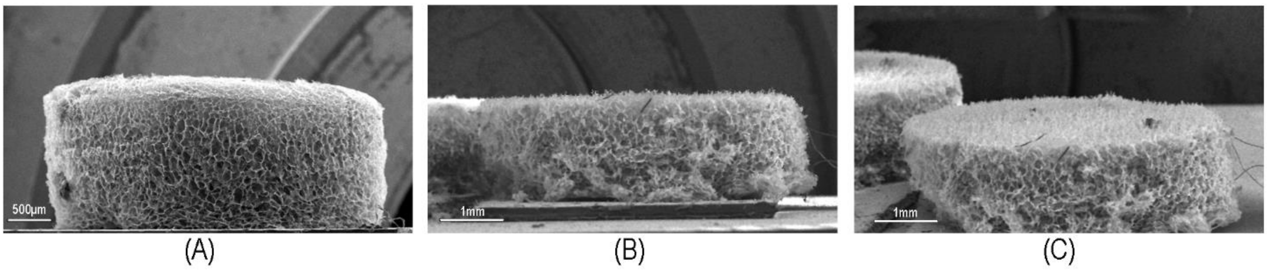

Figure 2.3.3.1-2: Flatten process of thick PCS. (A) 2mm PCS before any laser fabrication or interaction. Side view photo. (B) >2mm PCS after the flatten process with laser fabrication. Side view

photo. (C) Same sample (>2mm PCS after the flatten process with laser fabrication) in 45° side view photo.

Experiments for estimating the axonal resolution r_z took place as following: After flattening, the PCS sample was cut in the middle via high-power beam (P=70 mW) starting from the top of the surface (z = 0) and moving until the bottom of the scaffold (z = 2000μm). In all experiments, laser beam, focusing on the initial focus for flattening and this place define as z=0. SEM images take with top view and side view, showing the structures on top of the surface but also inside the material.

2.3.3.2. Scanning Electron Microscopy

Micro-fabricated features on PCS were visualized by scanning electron microscopy (SEM). Imaging was performed on a JEOL 7000 field emission scanning electron microscope using 15 kV acceleration voltage [42]. PCS can be characterized with no coating and no preparation before imaging. Samples were stabilized on glass microscopy slides and placed with a double tape (3M 4016 Natural PUR Foam Double Sided Tape, 1.6mm Thick, 19mm x 13.7m) on the stage of microscopy.

2.3.3.3. Quantification of ablation radius

In order to quantify the radial and axial resolution of PCS ablation, r_r and r_z respectively, SEM images were analyzed by open-source image processing software. Top and side view SEM images of the microfabricate scaffolds were processed using the distance tool of the ImageJ software (National Institutes of Health, Bethesda, MD, USA).

2.4. Results and Discussion

2.4.1. Radial Radius of Ablation

In order to characterize the radial resolution r_r of ablation, specific 2D features sketched in the paint software were laser ablated. Features consisted of lines at different distance and squares with pixel size 10 μm, to estimate the limit of laser ablation on the top of the PCS surface and to measure the thickness of fabricated line features, which equals approximately $2r_r$. Features were produced using laser beam of P = 10, 20, 30 and 40 mW mean power. **Figure 2.4.1-1** shoes SEM images of PCS microfabricated at 10mW and 40 mW. The minimum achievable size of any structure have to be the laser beam size of the minimum power but above the threshold power. As we increase the laser power, the width of the structure is increasing too. If this width be measure for different values of power then the correlation between laser radial resolution and power can be accomplished.

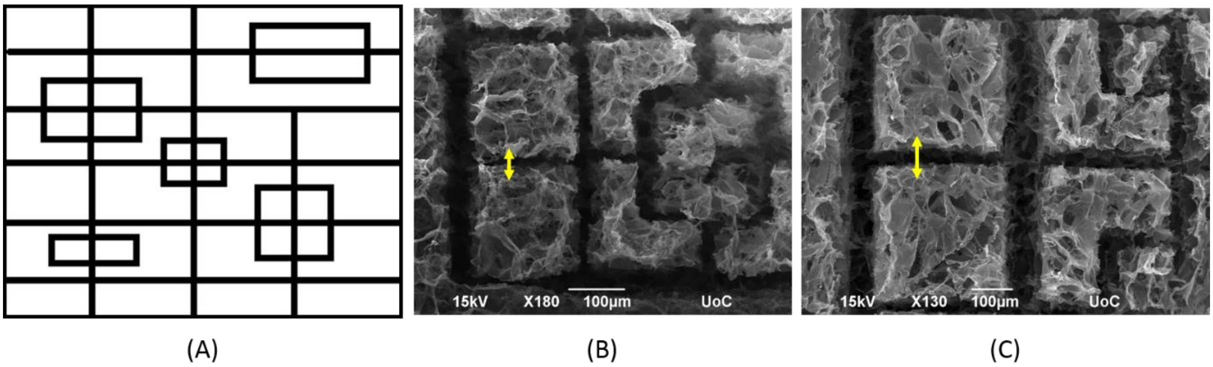

Figure 2.4.1-1: Experimental measurement of radial resolution r_r. (A) 2D figure sketch that laser beam will follow to ablate on the top of the PCS surface. Ablate line pattern on scaffold surface (B) with $P = 10$ mW and (C) with $P = 40$ mW.

Line ablation experiments conducted using laser beams of 10, 20, 30 and 40 mW show that radial resolution r_r is an increasing function of mean laser power P, see **Figure 2.4.1-2**.

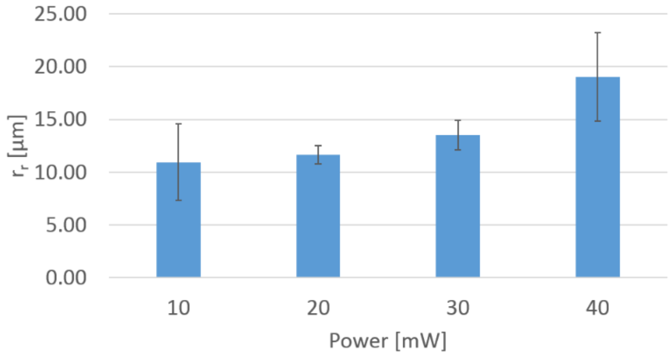

(A)

Power [mW]	r_r [µm]
10	10.95 ± 3.64
20	11.65 ± 0.85
30	13.52 ± 1.39
40	19.02 ± 4.18

(B)

Figure 2.4.1-2: (A) Effect of power on radial resolution. (B) Radial radius of laser of power respectively.

The effect of stage velocity U on radial resolution r_r was then examined by repeating the fabrication of the line patterns shown in **Figure 2.4.1-3-(A)** using stage velocity $U = 1$, 2 and 5 mm/s and mean laser power $P = 10$, 20, 30 and 40 mW. The results of this experiment, **Figure 2.4.1-3**, show that there is no statistically significant effect of stage velocity U on the radial resolution r_r of PCS microfabrication.

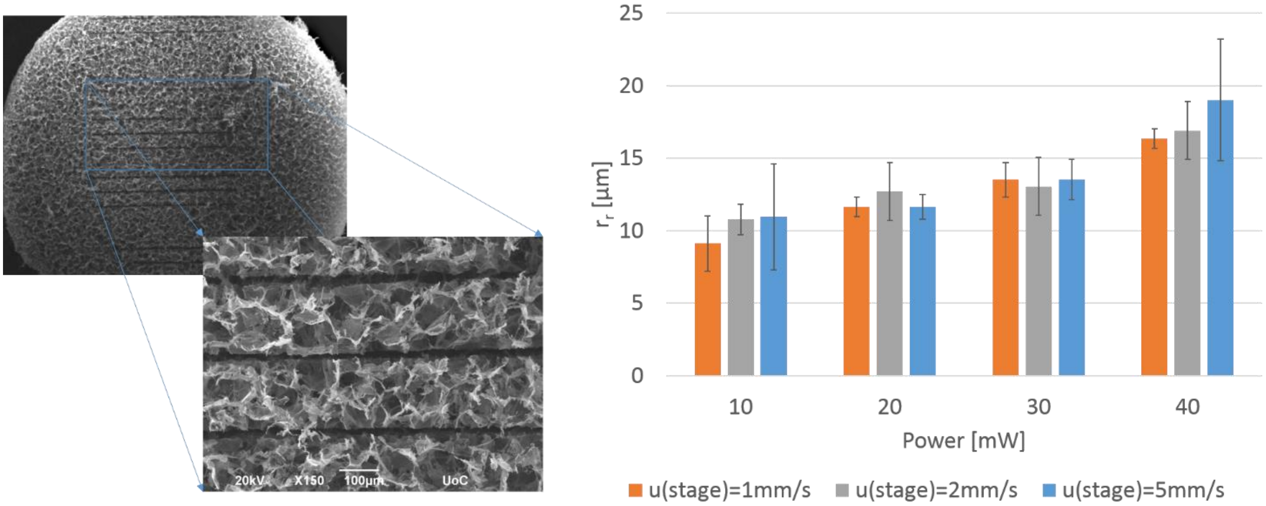

(A) (B)

Figure 2.4.1-3: Effect of stage velocity on radial resolution in different values of power. (A) Lines structuring on the top of the surface of PCS (magnification of structure) (B) Graph showing no significant effect of stage velocity on radial radius.

2.4.2. Axial Extent of Ablation

A particular interesting feature of PCS fs Laser ablation is that material removal can take place both on the surface and inside the PCS. It was of interest to generate a map of critical parameters that can result in either surface ablation or ablation inside the PCS **Figure 2.4.2-1**. Analytical calculations **[Section 2.2]** predict that the extent of ablated volume along the axial direction will be greater than the radial direction ($r_z > r_r$). Therefore, another major goal was to characterize the radial resolution r_z of ablation as a function of key parameter. Finally, apart from measuring r_z, it is of interest to observe if it is possible to achieve material ablation inside the PCS and not on the surface.

In process of characterizing axial ablation, a major challenge was the need to quantify axial radius. This challenge emerged from two reasons: First, the porous nature of PCS complicates measurements of features. Second, estimation of axial radius requires knowledge of the axial location of the focus plane from the material surface. The later was not known. Instead, what was known was the distance z of the current laser focus from the plane where PCS flattening took place. Therefore, a new variable was defined, ΔH based on the initial position z = 0 of flattening process (flattening at 40 mW). The samples were placed on the stage as was described in **[Section 2.3.3]**. After coarse manual focusing on the PCS surface using the CCD, PCS were flattened at $P = 40$ mW. This processed defined z=0. In later ablation steps, the stage moved along the vertical z axis and the laser beam ablated line features. SEM images of the resulting features were then utilized to quantify the h and H sizes. h was defined as the height of structure, defined as the difference of maximum minus minimum feature depth. H was defined as the maximum depth of the cut feature. Illustrate of the process, present in figure. After experiments, SEM images show results of radial cut resolution.

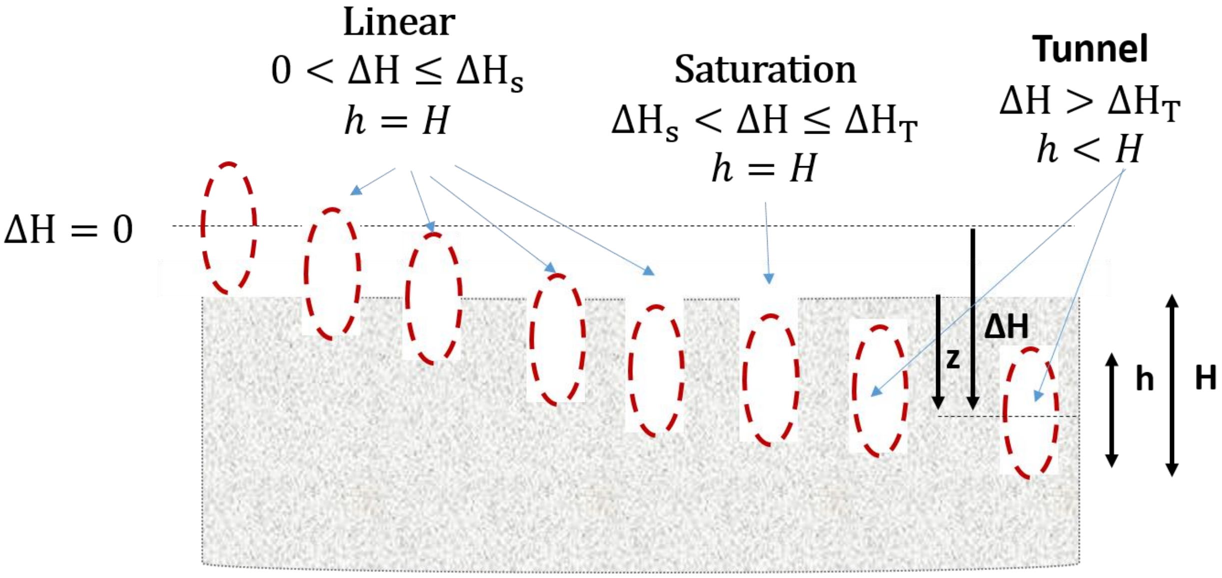

Figure 2.4.2-1: Theoretical figure of the experimental method on axial resolution measurement. Initially, the material was flattened and the position ΔH = 0 of the focus of the laser was defined in this position. Then the focusing plane approaches the material and focus inside the material. At each level, a 100 μm wide surface is cut using the same laser power. In the end, from SEM images (in side view- cross section) were measured the parameters H and h. H represent the maximum height-depth from the surface to the end of the structure and h is the minimum minus the maximum depth of the structure.

Experiments of ablation cut radius r_z utilized as main experimental parameters the mean laser power P and the vertical position of focus plane z. SEM images provided quantifications of h(ΔH) and ΔH(ΔH) for given laser power $P = 10$, 20, 30 and 40 mW. Overall, SEM images reveals that the spatial behavior of laser ablation can be classified into four regions: No ablation region, linear region, saturation region, and tunnel formation region, **Figure 2.4.2-2**.

Depending on the laser power, there is an initial range of z where no cut is observed. This considered to be the point where the beam is less than the focal point (located above). The beam is in the position of the original plane where there is no material at all since it is removed during flattening. As we proceeded to the inside of the material (z increases), we saw the reduction and degradation of the material. As the beam advances inside the material, larger axial cut depth - diameters are observed. The area representing this cut is linear. Saturation in the cut size is then observed. The exact reasons of this saturation are not completely understood. Finally, in the fourth region, a tunnel forms inside the PCS. Here tunnel refers to ablation of a volume inside the PCS that may not be visible from the PCS surface. A simulation of these results shows in figure with the equation that quantify H, h in different ΔH stage displacement **Figure 2.4.2-3**

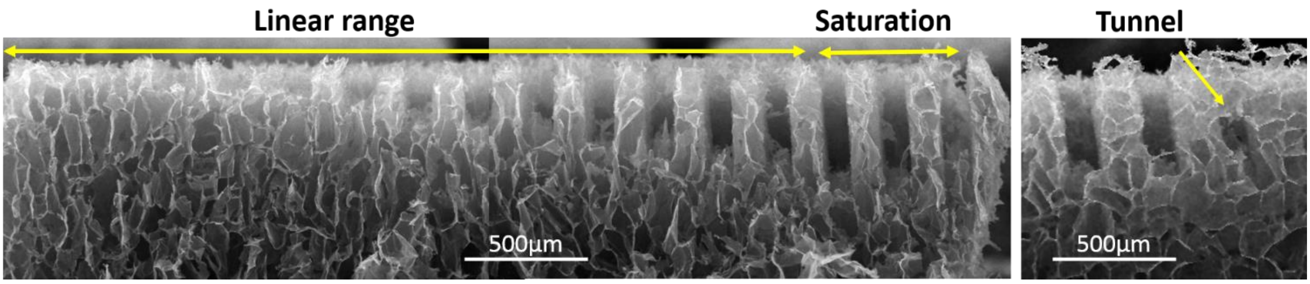

Figure 2.4.2-2: Four regions of radial resolution on thick PCS. SEM side view images.

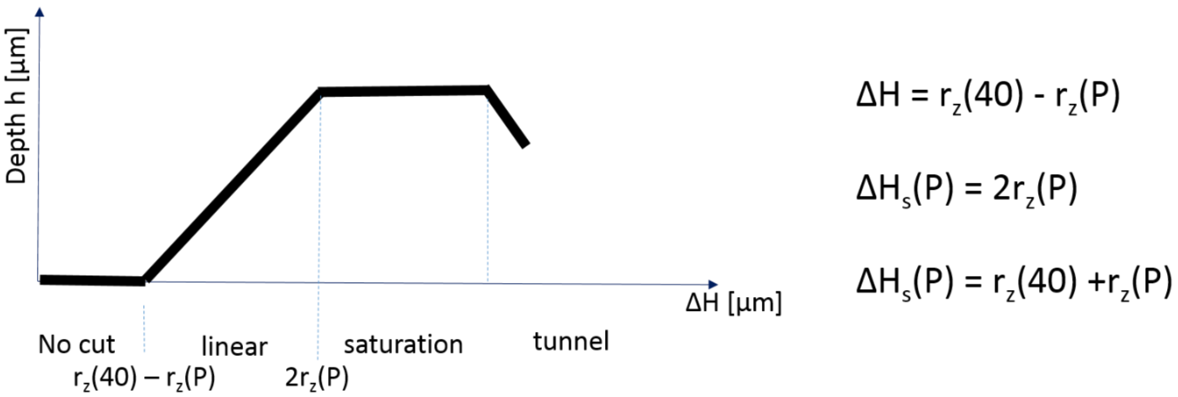

Figure 2.4.2-3 : Simulation of four regions. Equations can calculate ΔH and radial resolution of rz of saturation region.

Figure 2.4.2-4 shows how the values of h and H vary as a function of ΔH for P = 40 mW. Unambiguous similarity with the **Figure 2.4.2-3**. As it observed, at specific z, where h<H, tunnels forms inside the material. Some of the results shows in figure with SEM images of top view and side view. As it look on top view no structures are observed and the top surface of PCS is unaffected but when the sample seen from cros-section in side view, a tunnel form. The top of the PCS surface not came to any ablation process in contrast of the inside material **Figure 2.4.2-5**.

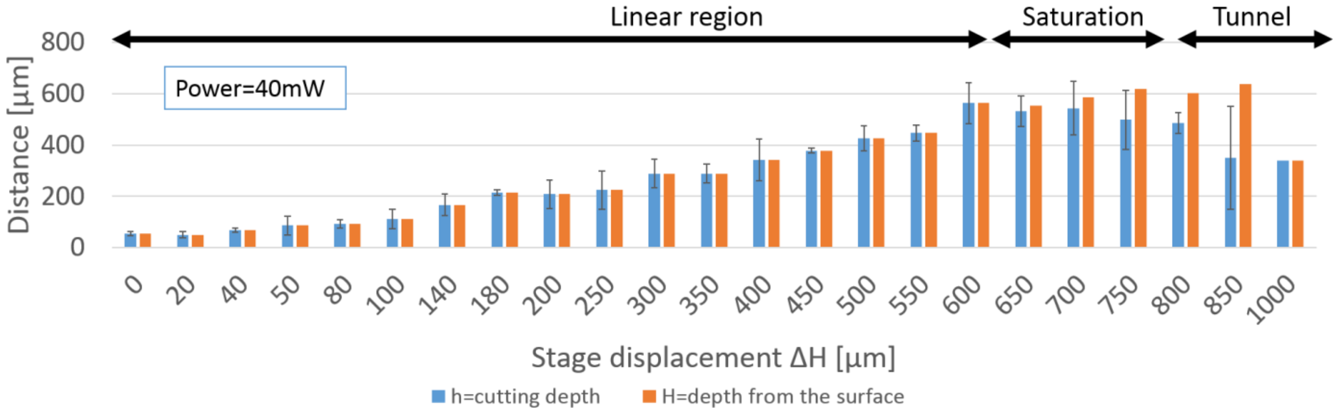

Figure 2.4.2-4 : Measurement of h and H cutting depth in dependence of stage displacement ΔH. Four regions make appearance.

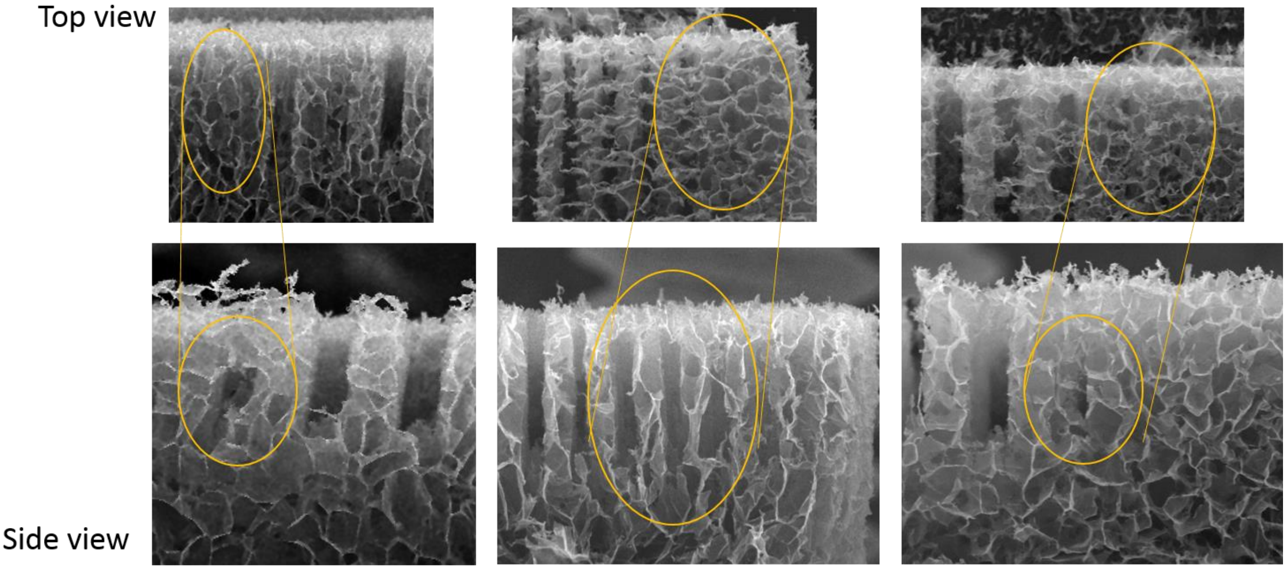

Figure 2.4.2-5: Tunnel formation. Structures make appear inside a material in specific ΔH depth focus. Power of irradiation is 40mW. SEM images.

We repeat experiments for radial resolution in a try to measure the effect of power on this cut. Using 30mW, 20mW and 10mW power in the same ΔH depth positions, results calculated and shown in different graphs below. Graphs shows the estimation of cut depth radius rz at P = 40 mW, 30mW, 20mW and 10mW respectively and will be described separately. According the equations:

$\Delta H = r_z(40) - r_z(P)$, $\Delta Hs(P) = 2r_z(P)$, $\Delta Hs(P) = r_z(40) + r_z(P)$, rz

and with the value of ΔH, which represent the real beam focus inside the material, calculate for each power the axial resolution of laser ablation.

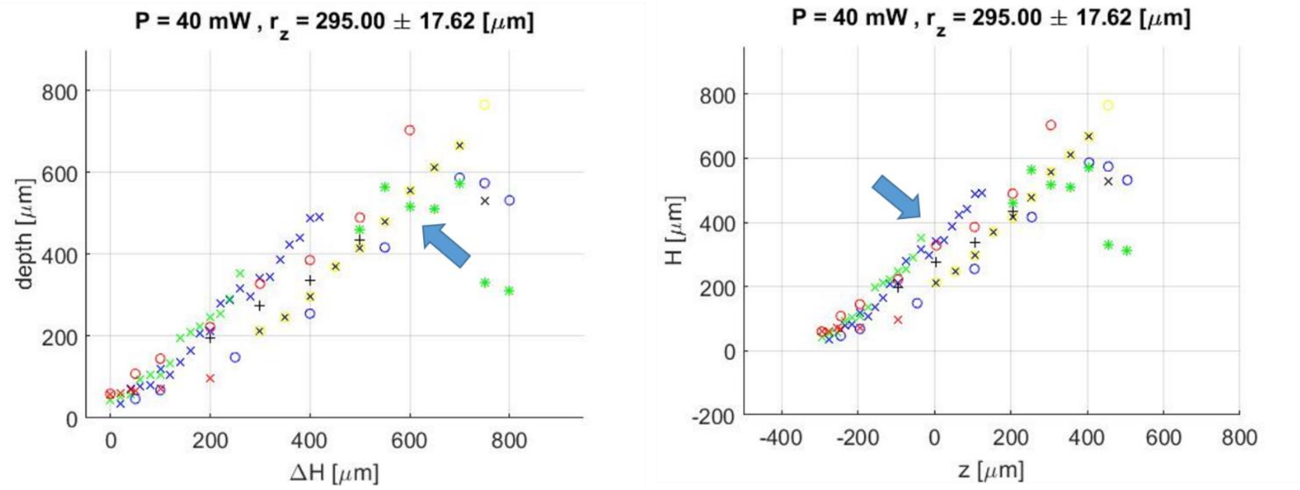

Figure 2.4.2-6 : Estimation of cut depth radius rz at P = 40 mW. Estimation gives r_z=296.0 ± 17.6µm for 40mW. All experiments of 40mW represent in this graph showing the four regions of ablation in different plane of z. Axial radius is calculated.

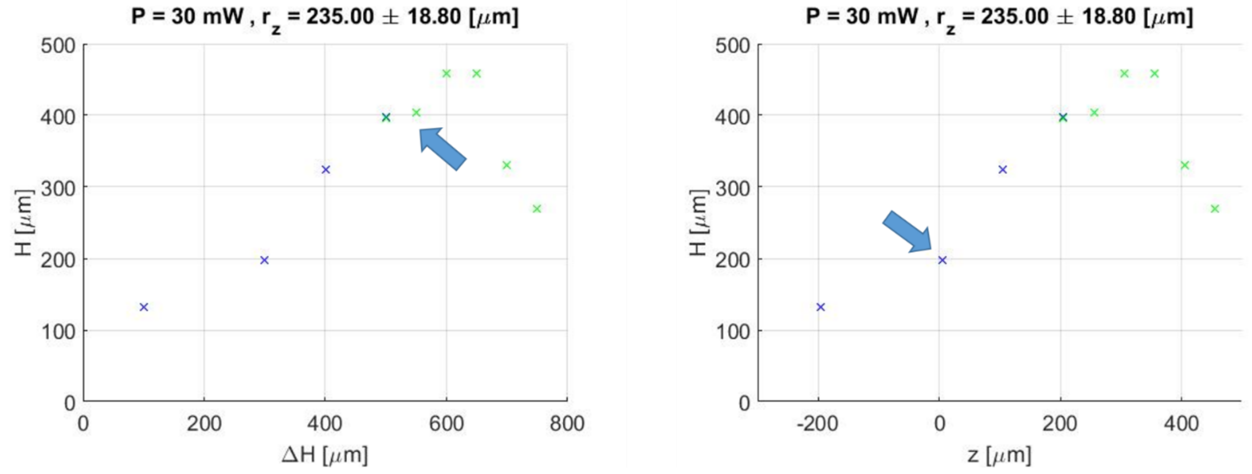

Figure 2.4.2-7: Estimation of cut depth radius rz at P = 30 mW. Estimation gives r_z=235.0 ± 18.8µm for 40mW. All experiments of 30mW represent in this graph showing the four regions of ablation in different plane of z. Axial radius is calculated.

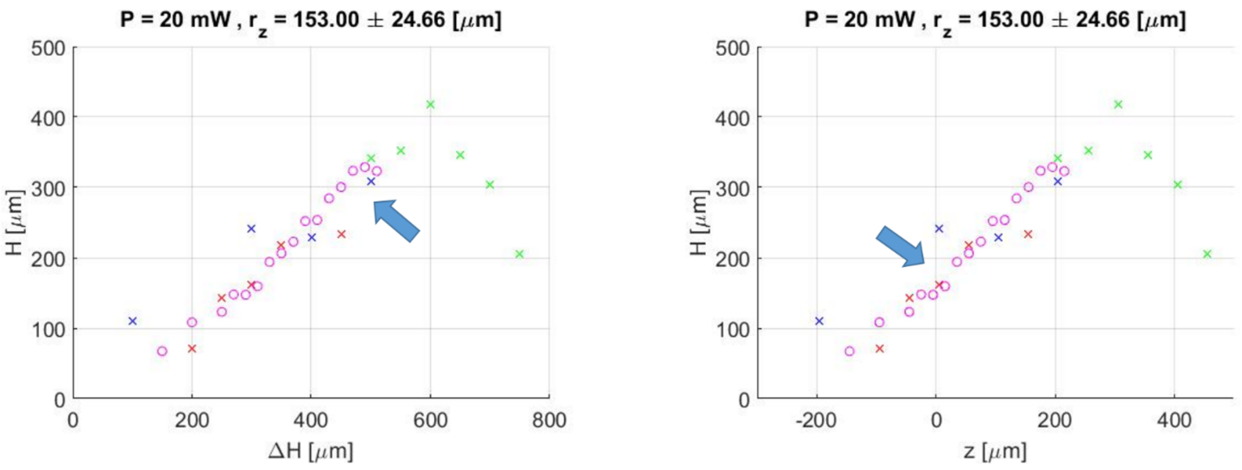

Figure 2.4.2-8: Estimation of cut depth radius rz at P = 20 mW. Estimation gives r_z=153.1 ± 24.7µm for 40mW. All experiments of 20mW represent in this graph showing the four regions of ablation in different plane of z. Axial radius is calculated.

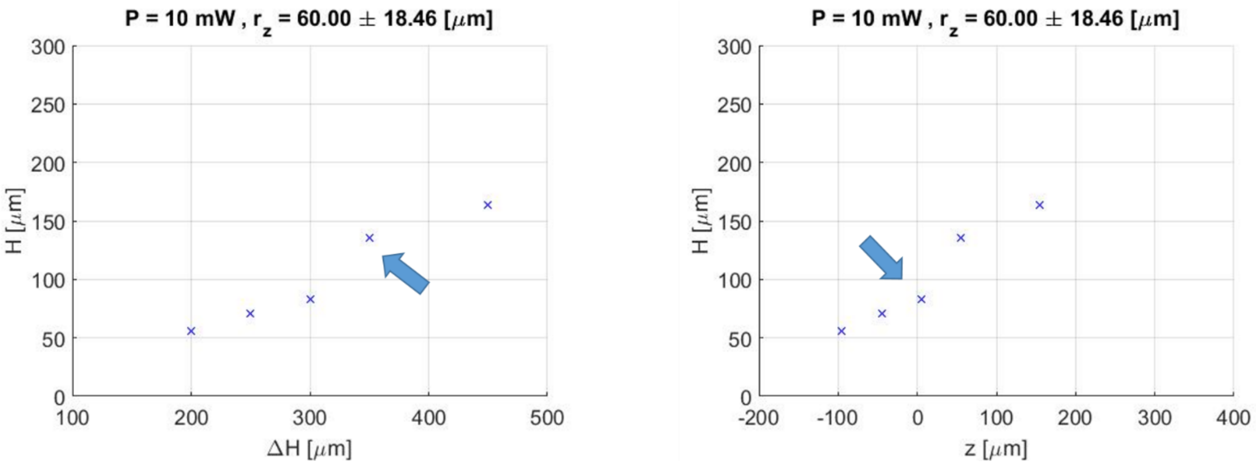

Figure 2.4.2-9: Estimation of cut depth radius r_z at P = 10 mW. Estimation gives r_z=60 ± 18.5µm for 40mW. All experiments of 10mW represent in this graph showing the four regions of ablation in different plane of z. Axial radius is calculated.

Estimation of cut depth radius r_z at different powers of all experiments represent and radial radius calculated in each power. The effect of power in radial cut resolution of radius is summed up in the table **Table 2.4.2-1**.

Power [mW]	ΔH$_s$ [μm]	r$_z$ [μm]
40	590.0 ± 35.2	295.0 ± 17.6
30	470.0 ± 37.6	235.0 ± 18.8
20	306.2 ± 49.4	153.1 ± 24.7
10	120.0 ± 37	60.0 ± 18.5

Table 2.4.2-1 : The effect of power in radial cut resolution of radius. Radial radius calculated in powers 40, 30, 20, 10mW.

Experimental results show that the square of the axial radius of beam is well described as a linear function of the power of the laser, in accordance with a simple mathematical model of ablation radius. Based on these calculations, it was estimated that the minimum laser power for ablation is slightly above 1 mW. Based on the theory and **Equation 2.4.2-1**, r_z^2 calculated and represents on a graph for several values of power analytically.

$$r_z^2 = \frac{2}{\pi \cdot NA^2 \cdot I_{th}} \cdot \mathrm{P} - \left(\frac{\lambda}{\pi \cdot NA^2}\right)^2$$

Equation 2.4.2-1

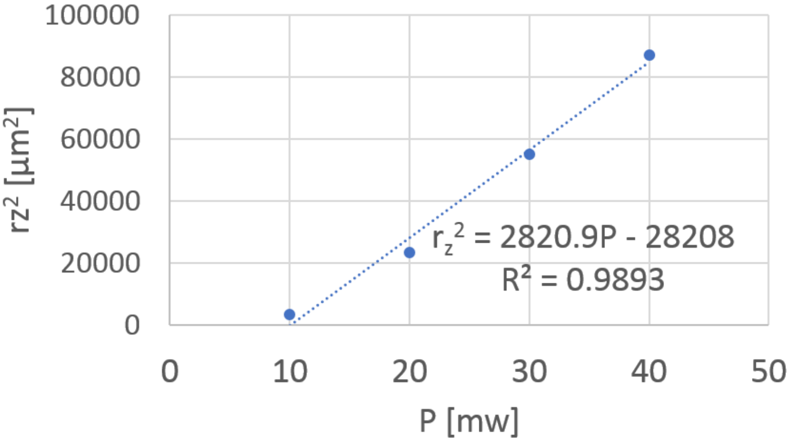

Figure 2.4.2-10: Effect of Power on Cut Depth Radius rz. r_z^2 in different values of power.

According the graph, $r_z^2(P)$ fit excellently to a linear line with the next equation.

$$r_z^2 = 2820.9P - 28208$$

Equation 2.4.2-2

Based on the parameters of this fit, key optical parameters of the system are estimated as $NA \approx 0.045$ and $I_{th} \approx 0.12 \frac{mW}{\mu m^2}$. Finally, the line of Equation 2.4.3 1 crosses the horizontal axis ($r_z = 0$) when $P =$1.2 mW. This estimation agrees with the experimental data of section XX that in the particular optical setup utilized, PCS ablation required mean laser power slightly above 1.2 mW.

2.4.3. Effects of Optical Parameters

2.4.3.1. Estimation of Ith

in order to estimate the intensity threshold I_{th} laser of increasing mean power was used to microfabricate a simple flat pattern on thin PCS, as described in **[section 2-2.3.3.1.1]. Figure 2.4.3-1**. Shows that as the mean laser power increases, the structures are fabricated on the PCS surface more clearly.

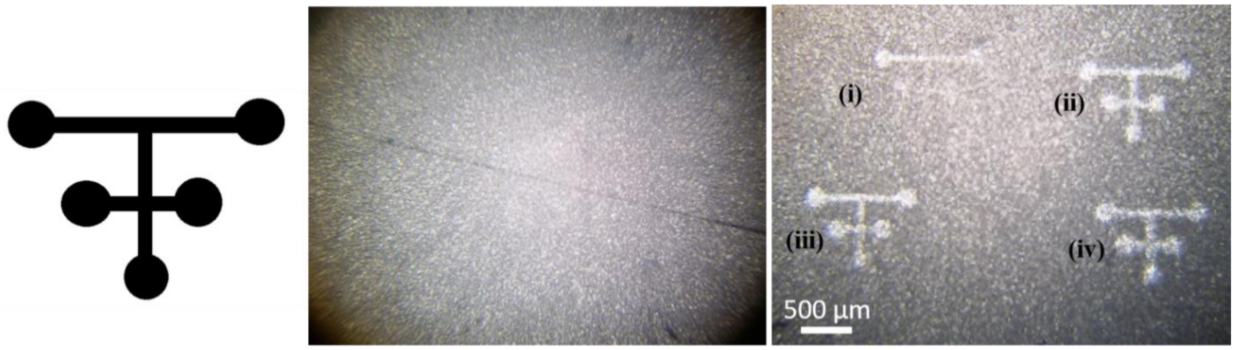

(a) (b) (c)

Figure 2.4.3-1 : (a) 2D figure sketched with paint program. (b) Thin PCS top surface with no structures observed when Power=1mW (b) Thin PCS top surface with structures (i) power=3mW (ii) power=3,5mW (ii) power=4mW (iv) power=5mW.

Based on these results, no ablation observed for P= 1 mW, incomplete ablation was observed when P = 3mW and robust ablation observed when P=4.5 mW. Based on these data, the ablation threshold was estimated between 1 and 3mW. The corresponding lower and upper bound of I_{th} can be estimated as $0.17 \frac{mW}{\mu m^2}$ and $0.5 \frac{mW}{\mu m^2}$ using the next equation:

$$I_0 = \frac{2 \cdot P \cdot \pi \cdot (NA)^2}{\lambda^2}$$

Equation 2.4.3-1

This result is in excellent agreement with the estimation $I_{th} \approx 0.12 \frac{mW}{\mu m^2}$ described in the previous section.

2.4.3.2. Effect of Mean Power and Stage Velocity

For variables power, new more complex figure have been used. That's way the accuracy could be checked and in the same time the resolution in each power. As the power increase, more clearly structures observed on the top of the surface and as it looks like the depth of each structure increases too respectively **Figure 2.4.3-2**. This is something we can observe because of the contrast between no ablated surfaces and ablated one. As figures below shows structured surface on power 20mW and 30mW are lighter than 5mW and 10mW. That's mean that structures on 20 and 30mW are deeper and go down to the glass surface than the others. As before no structure and no ablation observed on 1mW power.

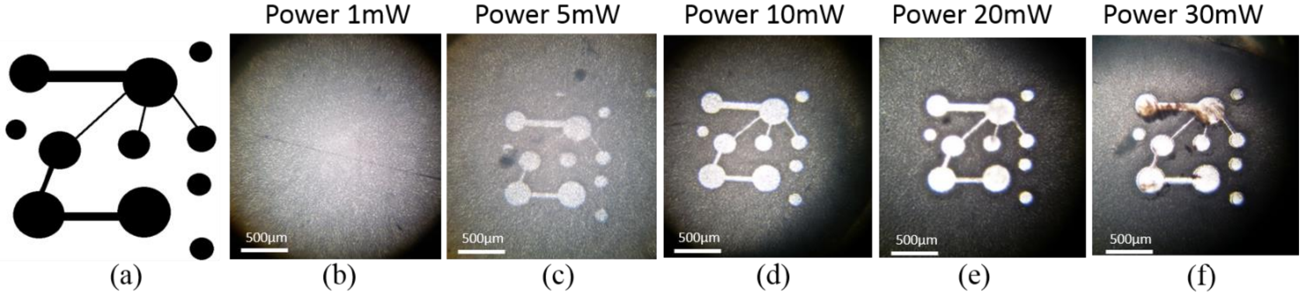

Figure 2.4.3-2 : (a) 2D figure sketched with paint program. (b) Thin PCS top surface with no structures observed when Power=1mW. Thin PCS top surface with (c) thin structures power=5mW (d) power=10mW (e) power=20mW (f) deeper structure power=30mW.

To study the effect of process velocity on the top of thin PCS, different values of stage velocity have been used. Power was stable on P=10mW and the only variable was the stage velocity. Stage moved in square figures from U = 0.5 mm/s to 12mm/s. Different contrast of images from simple microscopy, shows that structures with height velocity, have less contrast and lead to less depth of structures **Figure 2.4.3-3**. No quantification happens for this experiments but it believed that the different images contrast of structures could happen because of thin PCS properties like porous size.

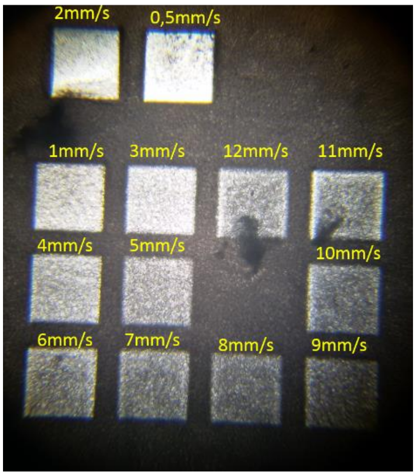

Figure 2.4.3-3 : Effect of the stage velocity on process ablation. Different values of stage velocity was used. P=10mW.

Chapter 3: Practical Implementation of Porous Scaffold Microfabrication

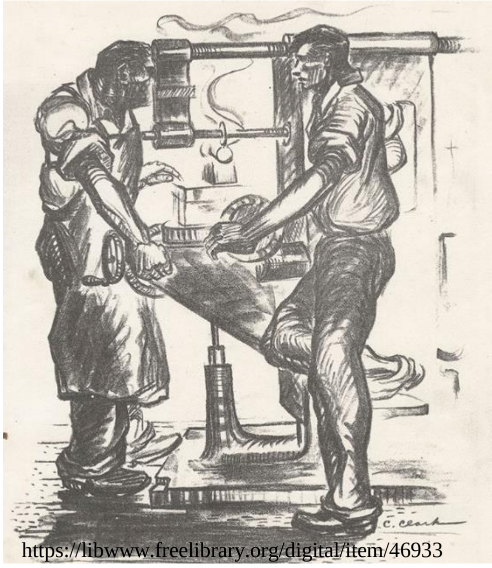

https://libwww.freelibrary.org/digital/item/46933

This chapter describes the implementation of PCS microfabrication by laser ablation in the laser facility of IESL-FORTH. Section 3.1 describes the processing pipeline and highlights differences and similarities between classical machining, 3D printing and laser ablation of PCS. Sections 3.2 and 3.3 describe the computer-aided tools (CAD and CAM) utilized. Section 3.4 briefly discusses how PCS were mounted on the micromachining setup. Finally, Section 3.5 provides examples of PCS microfabrication, while Section 3.5 includes the samples results and characterization

3.1. Introduction: PCS Microfabrication Pipeline

3.1.1. Fabrication Pipeline in CNC Manufacturing Processes

Traditional manufacturing processes for metals, plastics, ceramics and composite materials can be classified into material removal processes (e.g. turning, drilling, milling), forming and shaping processes (e.g. abrasion, bending, rolling, wire drawing) and casting (Kalpakjian 1995). The choice of appropriate fabrication method depends on the material to be processed and the desired specifications (dimension sizes, dimensional tolerances, surface finish, smallest feature size, component temporal loading profile) of the component of interest. This thesis utilizes fs laser ablation as a novel means to fabricate micron-sized features in porous collagen scaffolds.

Over the past twenty years several novel laser-based manufacturing technologies have emerged including additive manufacturing (e.g. 3D printing) and laser ablation. Such processes utilize lasers in order to progressively remove (e.g. by ablation) or add (e.g. photopolymerization) material. Such laser-based manufacturing processes can provide high-performance in terms of precision and repeatability and in terms of the nature of materials that can be processed.

Regardless of the manufacturing process chosen to fabricate a component (sometimes a cascade of processes is required), modern manufacturing systems utilize computer-driven machine tools to improve repeatability and precision. Computer-numerical-controlled (CNC) machine tools utilize computer-controlled motors that define the position/orientation of the stage (where the sample is held) or the tool (used to add or remove material). In CNC machine tools, motor motion is accurately controlled using closed-loop control systems in order to track specific paths. These paths are usually generated automatically based on 3D drawings of the component to be fabricated.

Figure 3.1.1-1 shows the pipeline utilized in contemporary manufacturing processes in order to convert ideas into a final component. This pipeline is common for both material removal manufacturing processes (e.g. milling) and additive manufacturing processes (e.g. 3D printing). The first step is the design of the component to be manufactured. This design process is highly problem-specific and its outcome depends on several constraints including budget, time and resources. A Computer-Aided Drawing (CAD) software is utilized to describe the geometry of the component in 3D space. CAD drawings are then processed by a Computer-Aided Manufacturing (CAM) software that generate low-level instructions that define the operation of CNC machine tools. The appropriate CAM tool depends strongly on the manufacturing process. Finally, the low-level instructions generated by the CAM software are loaded into a CNC machine tool and implement the manufacturing process that provides the final part.

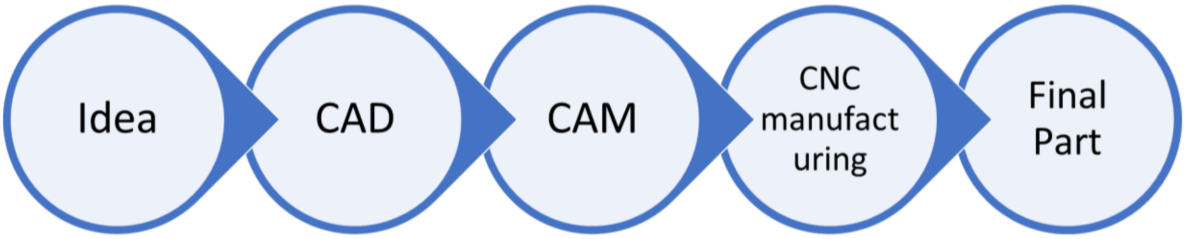

Figure 3.1.1-1: Contemporary manufacturing pipeline for turning an idea into reality. Initially, CAD software is used to develop a 3D representation of a desired part/component. The CAD file is then processed by a CAM software that generates the elementary instructions that define the motion of the specific computer numerical controlled (CNC) machine tool that will manufacture the part. The instruction sequence generated by CAM software controls the CNC machine tool during the manufacturing process in order to provide the final part.

While the pipeline described in **Figure 3.1.1-2** is valid for both material removal processes and additive manufacturing processes, there are some key differences. CAM tools for material removal processes consider in detail the configuration of the machine tool and the initial dimensions of the raw material in order to generate 3D paths for the part and the cutting tool. CAM tools for additive manufacturing convert a 3D object into multiple thin layers to be print layer-by-layer. In each layer, the path of the printing head is 2D.

Each material removal processes can be divided into three steps: first, high-feed machining removes large volumes at low precision. Then, a series of cutting "passes" removes progressively material and provides a component close to final desired shape. Finally, a low-speed finishing stage ensures high-precision machining and provides a component that meets the desired specifications on dimensional accuracy and surface quality. During an additive manufacturing processes, the volume to be printed at each layer is divided into the outside contour (that defines the outer surface of the component) and the inner part.

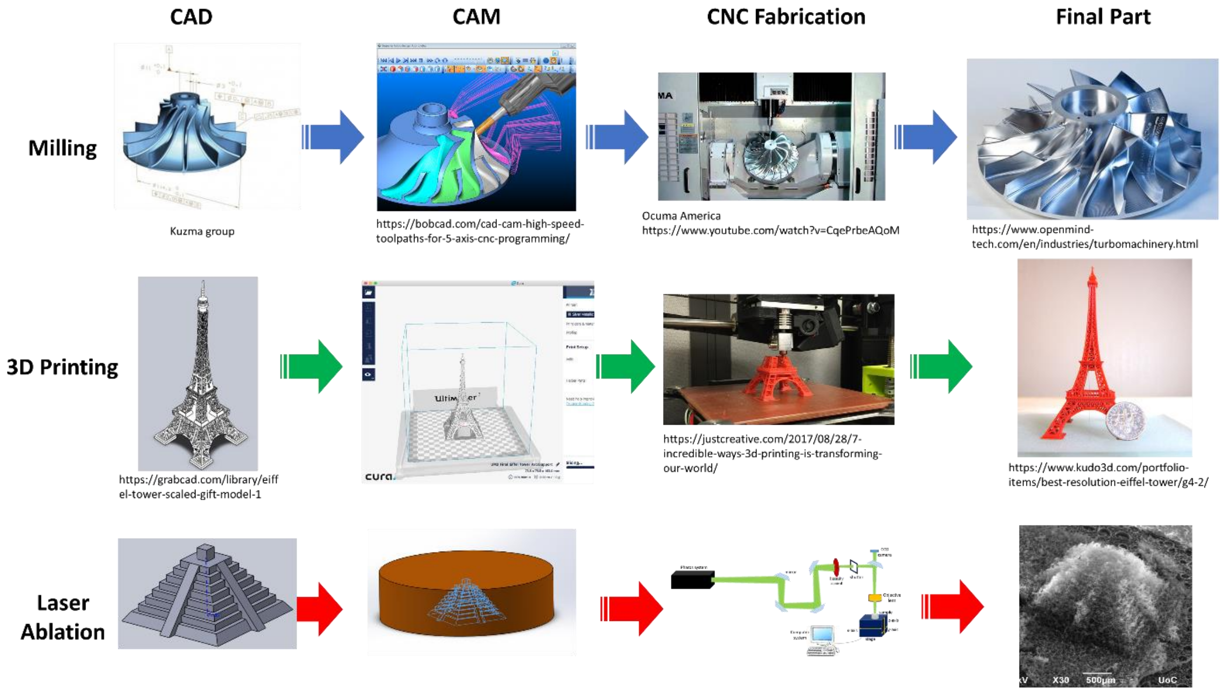

Kuzma group

https://bobcad.com/cad-cam-high-speed-toolpaths-for-5-axis-cnc-programming/

Ocuma America
https://www.youtube.com/watch?v=CqePrbeAQoM

https://www.openmind-tech.com/en/industries/turbomachinery.html

https://grabcad.com/library/eiffel-tower-scaled-gift-model-1

https://justcreative.com/2017/08/28/7-incredible-ways-3d-printing-is-transforming-our-world/

https://www.kudo3d.com/portfolio-items/best-resolution-eiffel-tower/g4-2/

Figure 3.1.1-2: In the case of a conventional machining process for the manufacture of a turbine, the CAM code controls the movement of the cutter to cut the wings of the turbine. In the case of 3D printing, the CAM program separates the object into several thin layers and creates the orbits that add the material. In the case of PCS microfabrication, the process is a combination of the two as a CAM tool for 3D printing was used to control a material removal process. In particular, after designing the component to be fabricated in a CAD program, the same program is used to determine the volume of the PCS to be cut. (This volume is entered into the Cura program which creates the laser tracks (respectively the stage) needed to make the cut.)

3.1.2. Fabrication Pipeline of Laser PCS Microfabrication

Laser microfabrication of PCS has several similarities and differences to contemporary material removal manufacturing methods and additive manufacturing methods. Laser microfabrication of PCS, just like conventional material removal processes (e.g. milling), generates the desired component by progressive material removal from an initial raw part. The 3-phase procedure (rough machining, main machining, finishing) utilized widely in metal machining can also be applied in laser microfabrication of PCS. However, a major difference of PCS laser ablation is that it can remove material from either PCS surface or inside a PCS. In contrast, material removal in conventional manufacturing processes takes place only in the component surface. Furthermore, during conventional material removal there is application of large mechanical forces into the piece, necessitating the tight mounting of the piece in the machine tool. In contrast, PCS ablation does not induce large forces to the piece, therefore mounting can be much more gentle and distortion-free. Compared to laser ablation in general, femtosecond laser ablation of PCS can achieve high beam accuracy and minimal thermal damage to the surrounding sample. Finally, several conventional material removal processes (e.g. milling) could not be applied to PCS (or several kinds of biomaterials in general) due to several reasons including sterility issues and poor machinability of scaffolds.

The specific pipeline utilized in this thesis for implementing 3D fs laser microfabrication of PCS is shown in **Figure 3.1.2-1**. The parts to be fabricated are designed in a CAD software (see section 3.2). A CAD drawing of the initial raw material is utilized to generate the volume that is to be removed by ablation. This volume is then processed in Cura, a free CAM software for 3D printing (Section 3.3). Cura slices the ablation volume into thin slices and generates the stage trajectories required to conduct the cut. The G code generated by Cura is loaded into a custom-written software (Andreas Lemonis, IESL-FORTH) that interprets G code commands into a series of simple motions of the stage where the sample is mounted during fabrication. The same software also controls the laser beam shutter. The user needs to mount the sample carefully on the stage **[Section 3.4]**, define the coordinate system axis and start the ablation process.

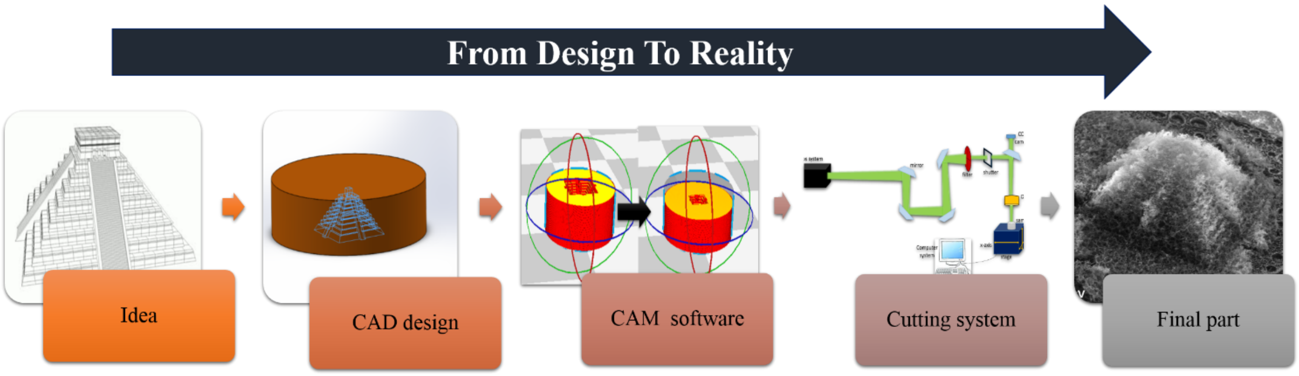

Figure 3.1.2-1 : PCS 3D fabrication. From the main idea of an object to the reality. A draw with a CAD software. This CAD model saved as STL file. STL file is opened in a slicing software which configures cutting settings and slice the object into layers with proper properties- settings. Each layer is made to a desired thickness and infill percentage, and then the layers are fused, one on top of the other, to form a full 3D shape from the 2D layers. In the next step file convert into a G-Code file and opened from the computer system on laser experimental setup and read as x-y-z stage movement. The ablation begins and PCS fabricate in this final 3D structures, giving figures with very good accuracy.

3.2. Computer Aided Design (CAD)

Based on the desired application and biological knowledge, the end-user of the microfabricated PCS needs to design a digital 3D representation of the object. Modern Computer Aided Design (CAD) software tools can be utilized to create digital descriptions of components of arbitrary complexity. CAD tools include complex packages utilized in engineering design such as Solidworks (Dassault Systèmes), Creo Elements (PTC), Inventor (Autodesk), AutoCAD (Autodesk) or simple publicly available tools such as Sketch-up (Last Software, Google). Alternatively, it is possible to design 3D objects using software utilized in the field of computer graphics and animation, such as rhinoceros (Robert McNeel & Associates) and Maya (Autodesk). Modern CAD packages enables engineers, architects, game developers or animation specialists to easily generate complex 3D objects via various tools, including the generation of 3D features (e.g. extrusions, holes etc).

Microfabrication of complex 3D objects and features in PCS requires a 3D representation of both the final desired “product” as well as an approximate 3D representation of the initial PCS sample volume. Since 3D microfabrication is a material removal fabrication process, the CAD designs can be saved in various file formats. Each CAD software package can save CAD drawings of parts or assembled parts using its own proprietary format (e.g. prt for ProEngineer, sldprt for Solidworks) or using universally-utilized open formats such as STL and IGES. Different CAD formats differ in the way they describe 3D objects. For example, an STL file describes the surface geometry of a three-dimensional object in the form of a series of triangulated surfaces. Furthermore, when a CAD drawing is produced in order to drive a fabrication process, the format chosen should be compatible with downstream computer-aided manufacturing (CAM) software tools, see section 3.3. Most CAM software packages can import and process universally-utilized CAD formats such as the STL file format. Therefore, in this thesis any CAD drawings generated were eventually saved as STLL files.

3.3. Computer-Aided Manufacturing (CAM)

Computer-Aided Manufacturing (CAM) refers to software tools that generate software commands that drive a computer-controlled machine tool (e.g. a milling machine, a lathe) in order to machine a specific component. The sequence of commands generated by CAM software, usually written in a specific programming language called G-code, drive computer-numerical control (CNC) machine tools, i.e. machine tools that operate based on closed-loop axis motion (in contract to manual machine tools, where the human operator drives each axis manually).

In this thesis, the components of interest were saved as STL files and processed by Cura, a free 3D printing CAM software. Cura performs two main tasks. First, it slices the 3D object into a series of layers. Such a “slicer” chops up a 3D model into many 2D layers (each one having a finite thickness). Second, for each layer, the program calculates the required path of the 3D printer head that will drive the 3D printer leading to printing the object of interest layer-by-layer. Cura is normally utilized for 3D printing, a manufacturing process where material is added progressively. However, in this thesis Cura was utilized to generate the paths (for each plane provided by the slicer) where laser ablation takes place in order to fabricate a specific component, i.e. a material removal process. Cura allows the user to perform several auxiliary tasks (object viewing and editing, scale object. locate object within printer space, highlight printer limits) and select settings (e.g. layer thickness, height, width and other properties, location of print start) given the 3D printer available. Table 3 shows the key parameters of Cura software, its meaning, and the values of each parameter utilized in this thesis. Based on these parameters, Cura slices the 3D volume to be removed into several thin layers (the number of layers depends on the object height and the value of parameter Layer Height **Figure 3.1.2-1**.

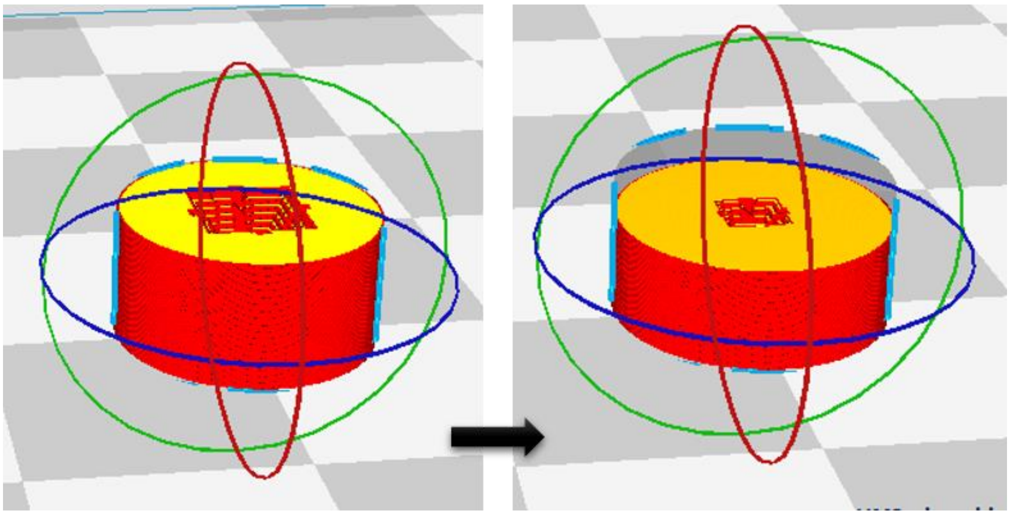

Figure 3.1.2-1 : Cura slices the 3D volume to be removed into several thin layers

Parameter	**Meaning**	**Value utilized**
Layer 0	On the top of the surface	See the sample in the plane
Layer n	Inside the material	See the sample in the plane
Layer Height	Distance between subsequent layers. This parameter should be chosen smaller than r_z	50 µm
Initial Layer Height	The first value (beginning)	1 µm
Line Width	The width of the line (laser beam width)	10 µm
Wall Line Width	The width of the limits around	100 µm
Infill Line Width	Limits around fill	0.1 mm

Wall Thickness	Thickness of limits around	0.1 mm
Infill Density	Density – thickness	50%
Infill Line Density	The distance between line to line (the value of this space)	0.01 mm
Infill Line Directions	The angle of writing – scanning direction	[0, 0] or [0, 90, 45, 40, ….]

Table 3.1.2-1 : Key parameters of the Cura CAM software, the meaning of each parameter in terms of a layer-by-layer fabrication process, and the values utilized in this thesis.

3.4. Sample Mounting

For high-precision manufacturing, it is very important that samples are stabilized well during XYZ stage movement. In each stage move, the PCS sample receives forces that induce its motion. These forces can adversely influence the cutting procedure. In this reason, samples of PCS are stabilized on the top of the stage with two ways. Samples were stuck using double-sided tape (Melca Double Sided Tape) on a Plain Glass Microscope Slides. Glass placed using double-side tape on the top of the surface. This stabilized the samples during the movement. In this case, after microfabrication, PCS samples can removed from the tape using a cutting knife and a tweezers, a procedure than can cause significant damage to the PCS sample. An alternative way is to stabilize samples on the top of a pipette tip (of 200μl volume). The tip stuck with double-side tape on stage. In this way the PCS sample can be reused with minimum lesions. After placed on the stage, the irradiation begins. These samples can be used later for biological application.

In 3D microfabrication only thick PCS were used because of their size (≈2 mm). Thick PCS are stabilized on the top of the stage with two ways. PCS samples stuck on the top of double-sided tape and placed on the movement stage. In this case, if samples must be used, they can be remove of the tape with a cutting knife and a tweezers. This may cause several damage of the structures. To avoid this the second way is to stabilize samples on the top of a pipette tip (of 200μl volume). In this way sample can be reuse with the minimum lesions. The top of the pipette tip was cut and stuck on the top of double-sided tape. All together were placed on the stage and the irradiation begins. These samples can be used later for biological application. In the case of 3D microfabrication the ununiformed of surface considered into final CAD design in order no flatten was needed before the experiment. First dimensions of the removal material design and then dimensions of the desirable object inside the material. In this way laser beam will remove the PCS (with the brown color of **Figure 3.1.2-1**) and will leave the object (with blue color of the **Figure 3.1.2-1**).

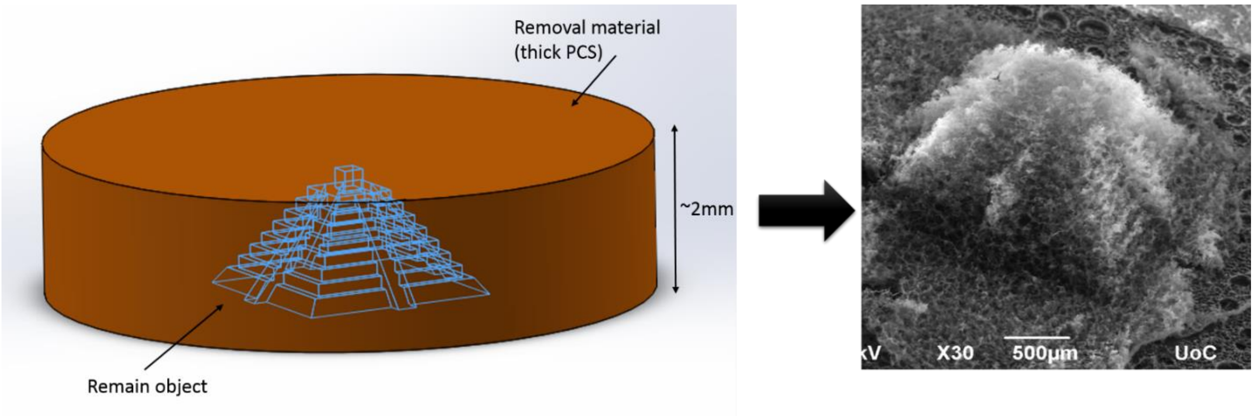

Figure 3.1.2-1 : CAD design of Aztac Pyramid. Brown color shows material that will be remove via laser ablation of thick PCS. Blue color shows the remaining object after the cutting ablation process. The result of this ablation is shown by SEM image.

In 3D laser microfabrication experiments laser power had been $P = 40$ mW and stage velocity was $U = 5$ mm/s. These parameters were chosen in order to minimize fabrication duration. However, laser microfabrication can be significantly improved by optimizing both P and U during the fabrication process. As the mean laser power decreases, the size of the ablated volume decreases too **[Section 2.2]**, providing structures of better accuracy. Alterations of stage velocity U will affect the processing time. The pros if this technique is the ability to have structures and object with the minimum size and the best accuracy with the less processing time, by changing the laser power. After the proper set of Power and stage velocity (depend on the aim), laser beam focusing on the top of the surface with a CCD camera, the point referenced with the ‘’set ref’’ button as z=0μm as explained in Chapter 2 2.3.3. and the ablation begins.

3.5. Experimental Results

Several 2D and 3D objects were fabricated using PCS microfabrication. 2D objects were fabricated in both thin and thick PCS. 3D objects were fabricated only in thick PCS.

3.5.1. 2D figures on thin and thick PCS

Various 2D objects were designed in CAD software and fabricated on the top surface of thin or thick PCS in order to verify the limitations of PCS microfabrication and provide scaffolds to be used for cell experiments on specific cell functions. Complicated objects used in order to study the radial resolution limitation and accuracy **Figure 3.5.1-1** on thin PCS. Microfabrication utilized mean laser power P in range 10 to 30 mW and stage velocity $U = 2$ mm/s. Images of the obtained structures were obtained via brightfield microscopy or SEM.

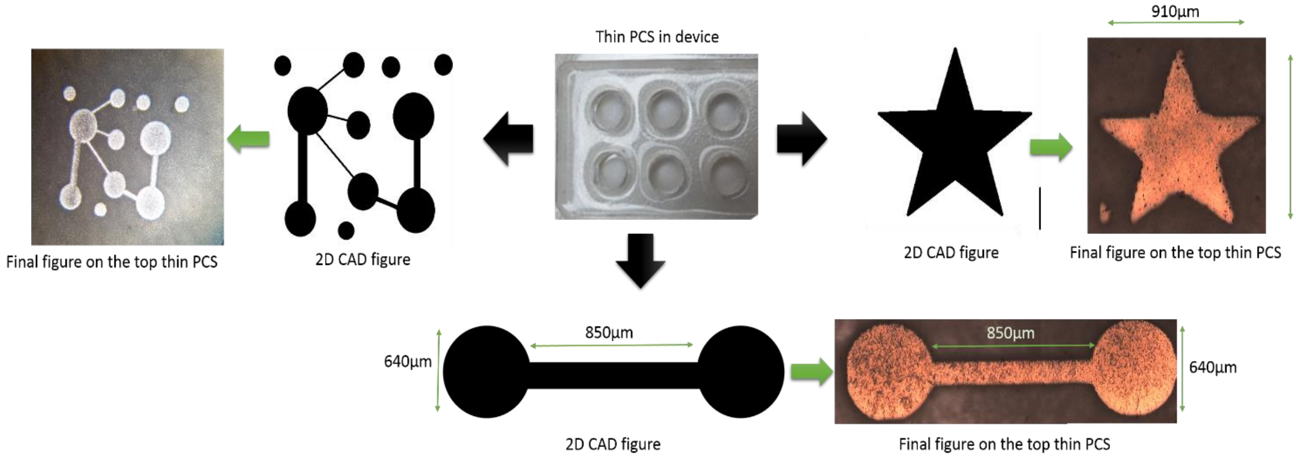

Figure 3.5.1-1 : Different 2D figures on the top of the surface of thin PCS. Device with thin PCS fabricated with 2D CAD design figures and gave the final structure with best accuracy. Power of these process was 20mW and stage velocity 2mm/s. Final structures photograph with a camera from a simply stereoscope microscopy.

The main idea for thick PCS were for future implants and fabricate structures that may can be used in many biological application. Results of these structures are in the figure below **Figure 3.5.1-2**.

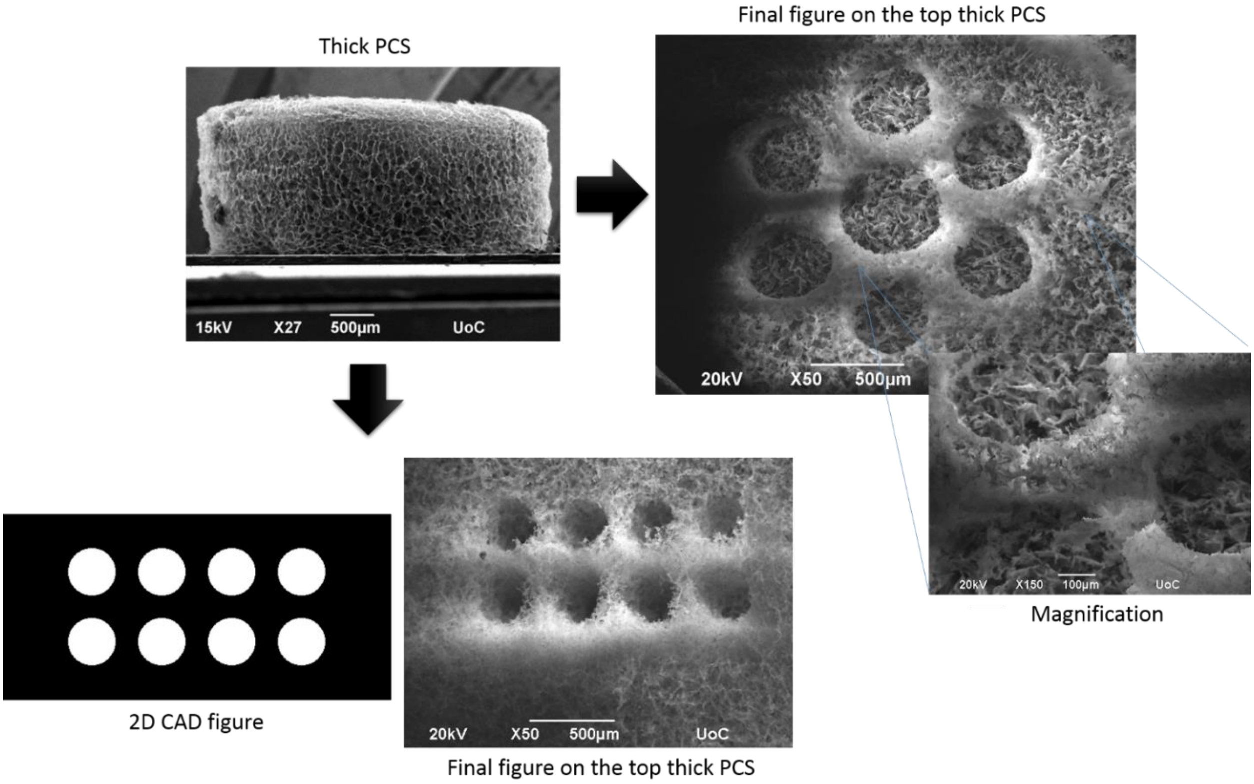

Figure 3.5.1-2: Different 2D figures on the top of the surface of thick PCS. Thick PCS fabricated with 2D CAD design figures and gave the final structure with best accuracy. Power of these process was 20mW and stage velocity 5mm/s. Final images from SEM.

Not only CAD program can be used but any black and white image can be used to computer program and transport to x-y stage movement during the ablation procedure. To demonstrate this capability, a photo of Prof. I. Yannas was utilized as a complex 2D object to be fabricated. Transportation of black and white images to x-y stage movement, gave accurate results in both thin and thick PCS, see **Figure 3.5.1-3**. The image of interest was fabricated on the PCS surface with high accuracy providing clear structures. In dependence of the cell experiment and study effect, the appropriate condition of ablation-fabrication have been used in any case.

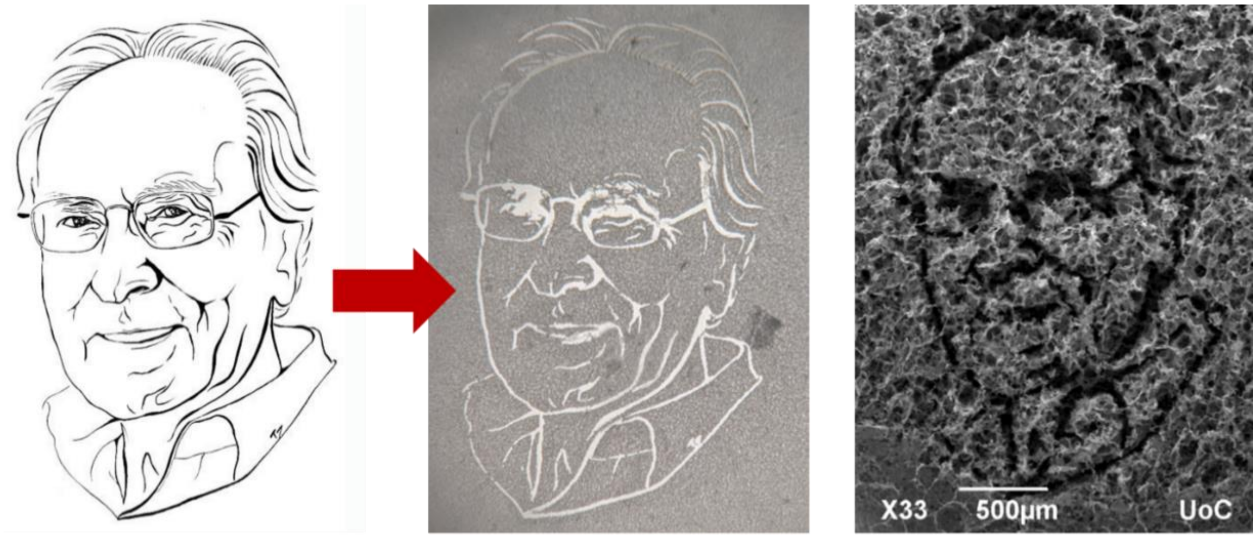

(A)

(B)

(C)

Figure 3.5.1-3 : Black – White picture can be used to computer program as a complex 2D object to be fabricated. An example of Professor Yannas photo. (A) Black white transportation into laser ablation on (B) thin PCS and (C) thick PCS.

Chapter 4: When Biology Met Microfabrication

This chapter emphasis potential biological applications of laser microfabricated PCS as a means towards manipulating cells fates. Focusing on the effect of topography on cells outgrowth with an early observation Section 4.1 provides an introduction on how microfabrication effect on cell function. Section 4.2 describes cell types utilized. Sections 4.3 and 4.4 provide the processing methods and results of experiments.

4.1. Introduction

A major challenge of tissue engineering and regenerative medicine is to mimick the complex cellular organizations and functions of native tissues. [43] The *in vivo* extracellular environment of cells, features both biochemical and physical cues, to which cells respond by initiating various intracellular processes [44]. Several studies suggest that matrix topography can affect cellular morphology, orientation and key cellular functions such as adhesion, proliferation, migration and differentiation [45]. Laser microfabrication via ablation enables precise surface patterning at the cellular and the subcellular scale to control cells functions of interest. Such surfaces have been widely used as cell culture platforms for the in vitro study of cellular responses on topographical cues [5].

4.1.1. 3D microfabrication of collagen as a means towards the manipulation of cell fate

Collagen has been widely investigated for use in nerve regeneration. It has been used in a variety of biomedical fields such as drug delivery carriers, surgical threads, bone healing material and wound dressing [46]. Even though type I collagen is not a principal component of the extracellular matrix (ECM) of the central nervous system, it can support the growth and differentiation of neurons *in vitro* and has been applied as a gel scaffold *in vivo*. Collagen I can also inhibit glial proliferation and thus may decrease glial scar post-spinal cord injury (SCI) [47] [48]. In peripheral nerve regeneration experiments, collagen implants have facilitated regeneration of severed axons to the level of nerve auto graft. Spilker et al., found that collagen tubes implanted across a gap defect in a rat spinal cord reduced the density of collagenous scar and aligned the reparative tissue with the long axis of the spinal cord [16].

4.2. Cells types

4.2.1. Cell culture

4.2.1.1. C2C12 Cell Line

C2C12 cell line is an immortal skeletal myoblasts line originated from thigh muscle satellite cells of female C3H mouse donor (Yaffe and Saxel, 1977; Blau et al., 1985). Proliferation of C2C12 occurs in growth medium that contains 20% fetal bovine serum (FBS). Under appropriate culture conditions (insulin supplementation, low serum) C2C12 cells differentiate into myocytes. Here, C2C12 were differentiated into myocytes using a medium that contains ITS (insulin-transferrin-selecium) medium supplement. Specifically, 100× ITS (Thermo fisher scientific 41400045) contains 1.0 mg/ml recombinant human insulin, 0.55 mg/ml human transferrin (substantially iron-free), and 0.5 μg/ml sodium selenite. Switching to differentiation media initiated C2C12 myogenesis 24-48h later, whereas fusion into myotubes takes 4-6 days. When 80% confluence is reached, AraC (1000X) is added to eliminate the differentiation process. The following day, medium is switched into differentiation medium (DMEM/h-g, 1% FBS, Eagle's medium nonessential amino acids, 0.25 mg/ml G418, Penicillin/Streptomycin, ITS). Medium is replaced every 2-3 days. Cells can be dissociated Trypsin or Accutase.

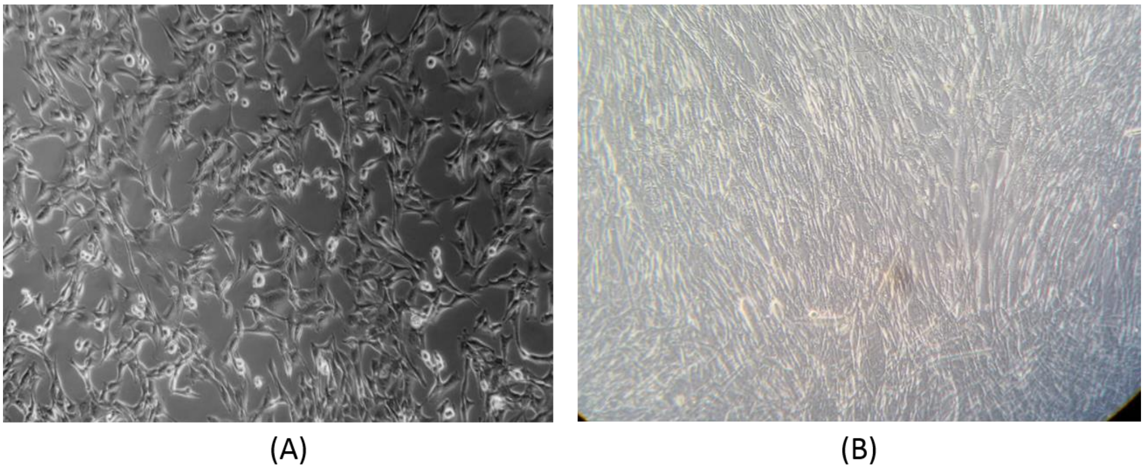

Figure 4.2.1-1: C2C12 culture. (A) Undifferentiated cell culture day 2. (B) Differentiated cell culture (visible myotubes). Images acquired by a 10X lens from a single microscopy.

4.2.1.2. NSC34 Cell culture and Differentiation:

Mouse Motor Neuron-Like Hybrid cell line (NSC34) is a hybrid cell line, produced by fusion of motor neuron enriched, embryonic mouse spinal cord cells with mouse neuroblastoma [49]. NSC34 cell line is used mainly to investigate pathophysiological mechanisms of motor neuron diseases like ALS. NSC34 cultures contain two distinct cell populations: 1) small, undifferentiated, highly proliferating cells and 2) larger, multi-nucleate motor-neuron like cells. NSC34 cells available at the IMBB-FORTH Neural Tissue Engineering Lab were a kind gift of Prof. P. Shaw (Sheffield Institute of Translational Neuroscience, U.K.). NSC34 cells are grown in proliferation medium (High-glucose DMEM, 10% FBS, 0.25 mg/ml G418, penicillin and streptomycin) until reaching 80% confluence. Then, AraC (1000x) is added to eliminate highly proliferating cells. The following day, medium is switched into differentiation medium (DMEM/F12, 1% FBS, Eagle's medium nonessential amino acids, 0.25 mg/ml G418, Penicillin/Streptomycin). Differentiation medium is replaced every 2-3 days. NSC34 cells can be dissociated by gentle pipetting. Dissociation of adherent cells does not require any dissociation reagent such as Trypsin.

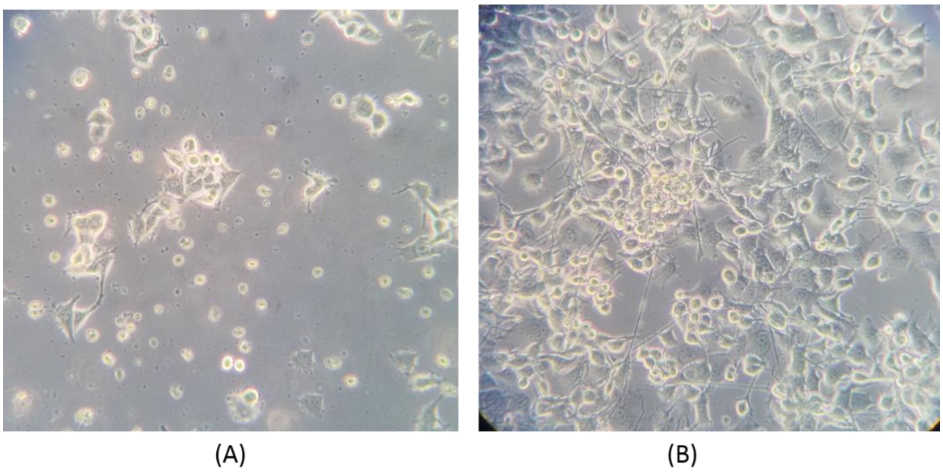

Figure 4.2.1-2: NSC34 culture. (A) Undifferentiated cell culture day 2. (B) Differentiated cell culture (visible neuronal axons). Images acquired by a 10X lens from a single microscopy.

4.2.1.3. Spheroid cell formation

It is important to design a system to co-culture different kinds of cells on the same scaffold, which allows the populations to interact, but also be easily distinguished. Consequently, the idea was to generate spheroids of one of the two populations, allowing easy separation, while supporting the 3D interactions within the cell sphere in different positions inside the scaffold. Cell spheres were generated by the hanging droplet method [50]. Briefly, cells were counted and suspended in 20% methyl-cellulose and 80% cell medium. For NSC34 sphere preparation, NSC34 proliferation medium was used. For C2C12 spheroid preparation, either C2C1 growth or differentiation medium were used depending on the type utilized C2C12. Each 25 μl droplet contained approximately 1000 cells. Droplets were placed on the lid of petri dishes. The dish was filled with 10 ml dH2O. Spheres were harvested next day and seeded into collagen scaffolds (protocol provided by G.Ziakas and O.Sarlidou).

4.2.2. Sample preparation

Cell co-cultures were performed inside thin or thick PCS. Both samples were sterilized before experiment by UV illumination for 30 minutes inside a biohood. After cell seeding, thick PCS were placed inside wells of a 96 well plate. Three types of cultures were examined: 1) single cell culture of differentiated C2C12 cells and differentiated NSC34 cells, 2) co-culture of differentiated C2C12 cells and NSC34 spheres, and 3) co-culture of differentiated C2C12 spheres and differentiated NSC34 spheres.

4.2.3. Cell Labeling

After four days of culture, C2C12 and NCS34 cells were stained with Calcein AM (Thermo fisher scientific C3100MP) to label live cells. The staining process realised after cells seeding on the scaffolds. In some experiments, C2C12 cells, stained before detachment from the growing substrate (Nunc™ Delta dish), with CellTracker™ Orange CMRA Dye (Thermo fisher scientific C34551) and thus excided red fluorescence. Specifically, in both cases, medium was removed from the dish and cells were rinsed once with PBS. Then, 2.5 μl dye was added in a 100μl serum-free buffer and added to the culture. After a 30 min incubation at 37°C, cells were washed two times with PBS. Finally, the PBS was replaced with fresh prewarmed media and 3 μg/ml Hoechst33342 nucleic acid counterstain stain (Thermo fisher scientific H1399) (blue fluorescence when bound to dsDNA) was added before imaging. Cell imaging was performed using the Operetta fluorescence microscopy system (IMBB-FORTH).

.

4.3. Method and Results

4.3.1. The effect of topography on cells outgrowth

Experiments were conducted in order to show that laser fabricated structures can control critical cellular phenotypes, such as their directionality, cell-cell and matrix-cell interactions, either in coagulation or singularity. In case of implants, thick PCS can be used in complex shapes to observe cell-cell interaction. Also thin PCS were used to study different in vitro biological aspects **Figure 4.3.1-1**.

Implants

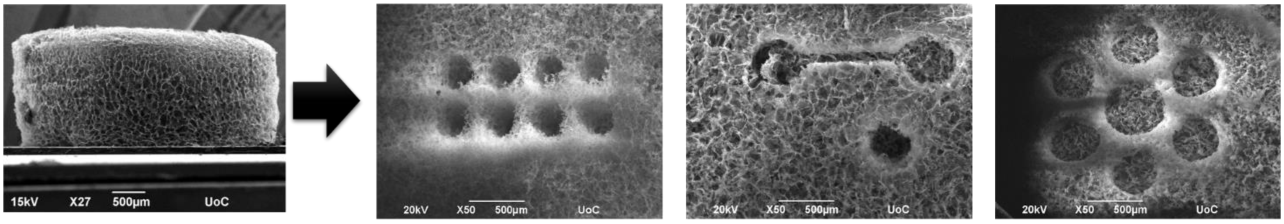

In vitro devices

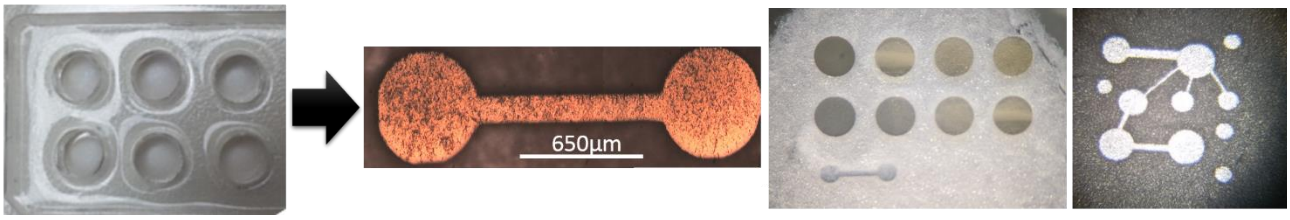

Figure 4.3.1-1: Different complex shapes according to the needs of the application. In case of implants thick PCS can be used. Also thin PCS in device can be used to study different in vitro biological aspects

Initially, laser microfabrication was utilized to fabricate lines on the surface of PCS and study their effect on cell directivity and outgrowth. Lines fabricated mainly to thin PCS **Figure 4.3.1-2** in order to observe the directivity of C2C12 cells. Differentiated C2C12 cells in concentration of 5000-6000 cells per well were seeded to thin PCS in the device as single cells in 100 μl C2C12 differentiation medium. Right after the C2C12 culture on Day 2, differentiated NSC34 cells (8000 cells per well, 100μl) were seeded in the same scaffold and the medium was switched to NSC34 differentiation medium supplemented with ITS. Cells were co-cultured approximately for 4 days to one week, depending on the experiment.

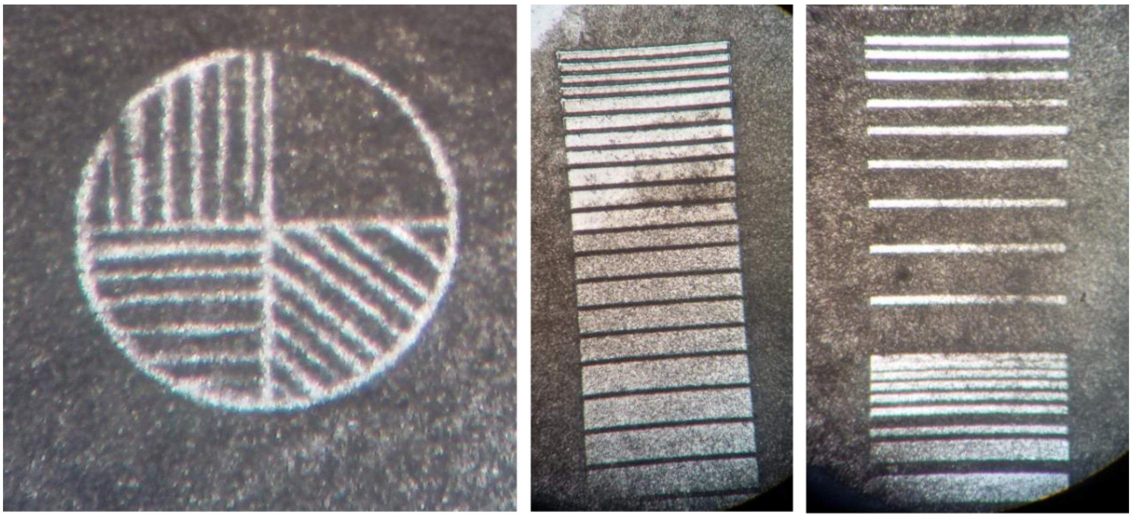
(A) (B) (C)

Figure 4.3.1-2: Thin PCS device: effect of angle of lines, width and distance between lines on cell's directivity and outgrowth

After 4 days of C2C12 cell culture, it was observed that cells were oriented around the structures following the direction of the features fabricated on PCS. C2C12 cells follow the microfabricated lines along their direction **Figure 4.3.1-3**. The important observation of cells in this experiment was also the fact that they liked the environment on these structures and they stay alive during the procedure.

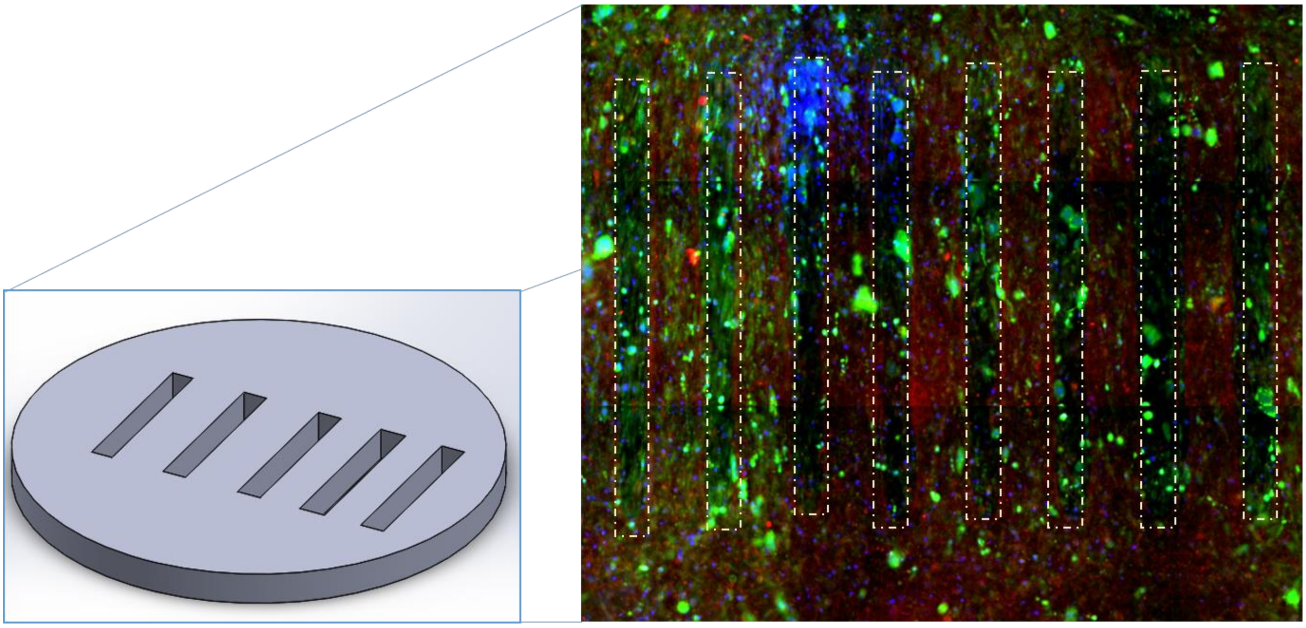

Figure 4.3.1-3: Effect of lines on cell directivity. After 4 days of C2C12 cell culture, it was observed that cells follow the microfabricated lines along their direction

Not only lines were fabricated but by constructing suitable wells and channels, we try to check the placement of cells inside the wells and the interaction between cells of the same or different type cells in co-culture **Figure 4.3.1-4**. We estimate that by changing the distance of the wells or even their size and shape, cell behavior changes. We placed targeted differentiated C2C12 spheres (5000 cells per sphere) and differentiated NSC34 spheres (8000 cells per sphere) into specific microfabricated wells of diameter 200 to 800 μm range. An amount of 10μl of total solution (cells and C2C12 dif. Medium) was targeted seeded into wells and channels.

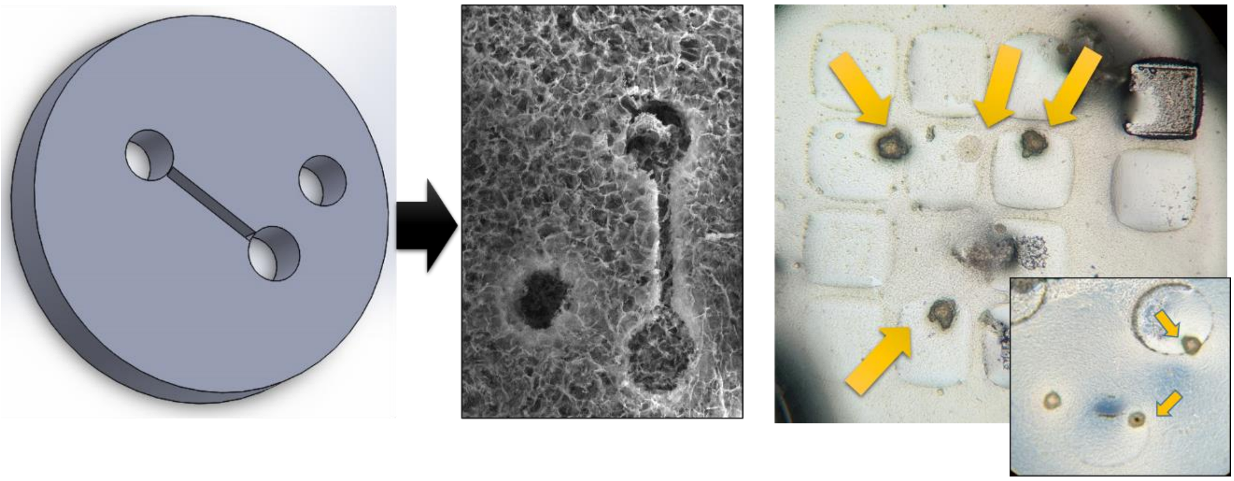

Figure 4.3.1-4: suitable wells and channels on thick PCS can be fabricate to check the placement of cells inside the wells and the interaction between cells of the same or different type cells in co-culture.

4.4. Discussion

Using the control of microfabrication we can take advantage of control cell directivity and interaction between different cell types. We can use this technology with porous collagen scaffolds and make structures for injures like optical nerve injury or spinal cord injury. Also making structures inside the material such as tunnel we can fabricate a system that may help in angiogenesis. One of the main features of vascular network is the delivery of all cells in tissue with sufficient nutrients. According the literature all cells in a tissue lie within 200μm from a vasculature. This is considered a general limit of diffusion of oxygen and nutrients into a vascular. In the case of PCS, the material is porosity and at the same time we can fabricate it in the micro scale of the order of 200 less and more [51]. To minimize vascular pressure, it is required that the vascular network be organized in the form of a tree where the larger pieces will be branched into smaller ones. An example of a vascular organization structure illustrate in **Figure 4.3.1-1**. OCT angiography in high-resolution images shows the outer retinal vasculature. This image with CAD program fabricated on the top of the surface of thin PCS. Endothelial cells will seed in the future. In order for the vascular implant to be easily associated with the vascular system of the patient, the vascular structures should have a diameter of up to 100 in accordance with the literature. Studies have shown that 20μm channel can positively support endothelial cells and succeed in making lateral vascular [52].

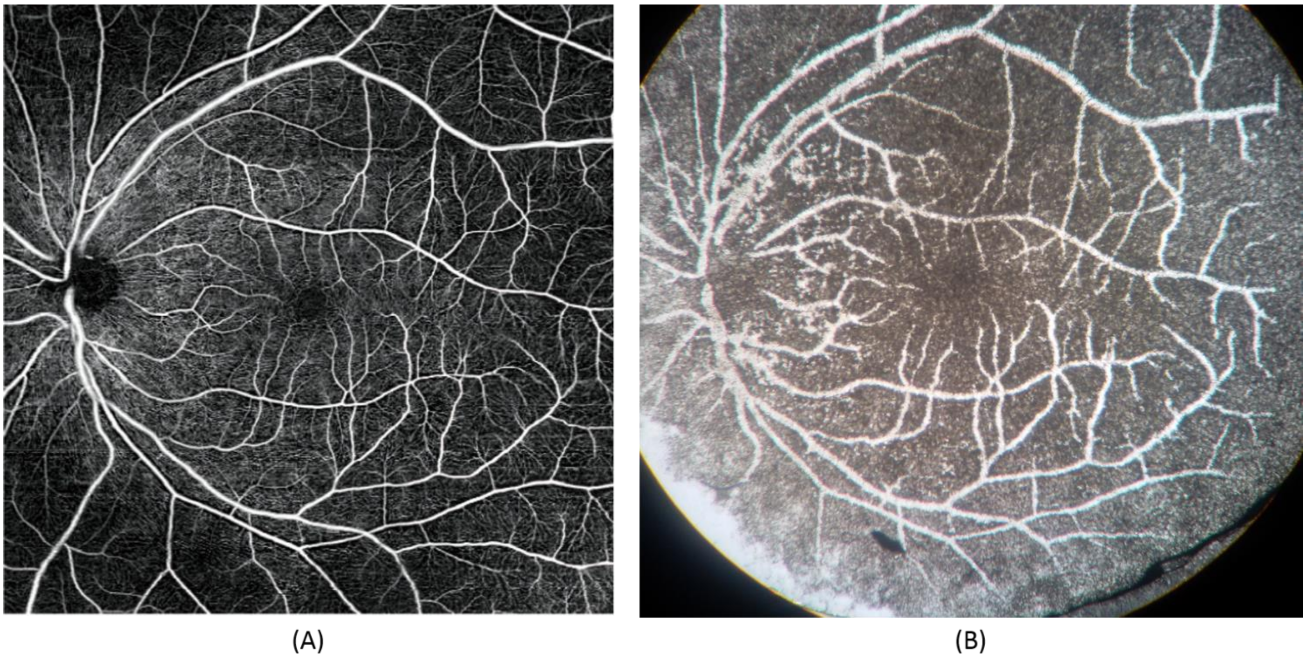
(A)
(B)

Figure 4.3.1-1: Example for a future angiogenesis model. (A) OCT angiography in high-resolution images shows the outer retinal vasculature. (B) This image with CAD program fabricated on the top of the surface of thin PCS.

Chapter 5: Conclusions and Future Work

5.1. Conclusions

This thesis belongs to the broad framework of bioengineering, the field that combines engineering, biology and physics to develop advanced methods that can promote both basic research and biomedical applications. In order to overcome the limitations of PCS fabrication via lyophilisation, a new process has been developed in this work, which can result in PCS of more complex shape and structure. This is achieved by using an ultrafast pulsed laser to remove material. In particular, fs laser was used because it has been shown that they can cut materials with high precision causing less thermal stress. Specifically, this thesis developed a new PCS microfabrication method using fs laser. It can provide a new biomaterial platform that will enable new cell culture devices, new implants and new tools for basic research cell studies. Based on simple Gaussian beam theory, it was estimated that the optical parameters influence the size of the ablated volume, assuming that the cut takes place in the volume where the light intensity exceeds a limit characteristic of the material. And I > Ith. Theoretical models of radial and axonal resolution show that cutting in the axial direction depends greatly on both optical and intensity of light. As laser mean power increases, the volume that is removed increases as the cut takes place more deeply away from the PCS surface. Conversely, the radial dimension of the cutting volume does not depend so significantly on our optics or power. Initially, the PCS were used to estimate the minimum intensity of the laser and noticed that for 1 mW power there is no ablation. Instead, ablation was observed for a power of 3 mW. Based on this measurement it was estimated that the light intensity threshold that causes cutting is just below 0.5 mW / μm^2. We also found that a prerequisite for the PCS system is to precede an initial cut which flattens its surface, which is initially curved. Experiments of radial resolution show that as the power of the laser increases from 10 to 40 mW, the diameter of the cutting increases from 10 to 17 μm. These results are consistent with the analytical model estimates that the radius of cutting in the radial direction depends, but not drastically, on the power of the laser. About the process effect (movement speed of the stage) during processing, show that did not significantly affect the radial dimension of the cut. It was observed that initially as the plane focusing the laser approaches and enters the material, the depth of the volume removed increases proportionally. However, after a region the cutting depth stabilizes. Finally, when Laser focuses on a given depth range within the material, the ablated volume is located in the inner part of the PCS. There is no cut in the surface just inside and tunnels form. In most experiments laser power was chosen at mW. To estimate the axial cutting radius, it was considered that the point at which saturation region appear, the depth of the removed volume equals approximately 2 axial cutting beams. Thus, for 40 mW laser power, the axial cutting radius was estimated as 295 ± 17 μm. The same experiment was repeated for laser power 10, 20 and 30 mW and the corresponding axial cutting radius was evaluated as 235 ± 19 μm, 153 ± 25 μm and 60 ± 18 μm respectively. Experimental results show that the square of the axial cutting beam is well described as a linear function of the power of the laser, in accordance with the simple mathematical model of a Gaussian beam. It was also estimated that the minimum laser power for cutting is slightly above 1 mW, in agreement with experimental findings. Finally, complex shapes according to the needs of the application can be fabricate with very good accuracy on the top of the surface and inside as well of the scaffold. In the final part of this thesis some simple biological experiments demonstrated that laser microfabricated structures on PCS can control critical cellular phenotypes, such as cell directionality, cell-cell and matrix-cell interactions, either in co-culture or singularity. Initially, creating line microstructures on the surface of PCS, it was observed that after 4 days of C2C12 muscle cell culture, the cells are oriented around the structures following the direction of the structures. An important observation is also the fact that our cells are impinging on these structures. By constructing suitable wells and channels, and specifically deep wells that can connected to each other by channels, we can check the placement of cells in topography and the interaction between cells of the same or different kind in co-culture. By changing the distance of the wells or even their size and shape, the behavior of the cells changes. Spheres cells can be used also.

5.2. Future Work

Future work can focus on optimizing the code that controls laser ablation. Biological experiments have to accomplish in order to study better the effect of microfabricated structures on cell directivity. Better mathematical model could be helpful in better explaining how optical parameters control PCS ablation and the limits of this manufacturing process. One idea is to consider light absorption and scattering by the PCS.

The developed technology for PCS laser microfabrication can provides structures inside PCS such as tunnel to break down an integrated system that may help in angiogenesis. Laser PCS microfabrication can construct complex structures both on the surface and on the inside of the material. In particular, internal structures such as tunnel can be used to create vascular systems, allowing the creation of pre-vascular implants adapted to the patient, a major challenge in regenerative medicineWe have to overcome a lot but one step once.

References

[1] I. V. Yannas, E. Lee, D. P. Orgill, E. M. Skrabut, and G. F. Murphy, “Synthesis and characterization of a model extracellular matrix that induces partial regeneration of adult mammalian skin,” *Proc. Natl. Acad. Sci.*, vol. 86, no. 3, pp. 933–937, 1989.

[2] E. A. Abou Neel *et al.*, “Collagen - Emerging collagen based therapies hit the patient,” *Adv. Drug Deliv. Rev.*, vol. 65, no. 4, pp. 429–456, 2013.

[3] I. V Yannas, “Tissue generation by Use of Glycosaminoglycan Copolymer,” *Clin. Mater.*, vol. 9, pp. 179–187, 1992.

[4] A. I. V Yannas, J. F. Burke, D. P. Orgill, and E. M. Skrabut, “Wound Tissue Can Utilize a Polymeric Template to Synthesize a Functional Extension of Skin,” *Science (80-.).*, vol. 215, no. 4529, pp. 174–176, 1982.

[5] C. Yiannakou, C. Simitzi, A. Manousaki, C. Fotakis, A. Ranella, and E. Stratakis, “Cell patterning via laser micro/nano structured silicon surfaces,” *Biofabrication*, vol. 9, no. 2, 2017.

[6] P. Weiss, “Experiments On Cell And Axon Orientation In Vitro: The Role Of Colloidal Exudates In Tissue Organization,” *J. Exp. Zool. banner*, vol. 100, no. 3, pp. 353–386, 1945.

[7] J. J. Norman and T. A. Desai, “Methods for fabrication of nanoscale topography for tissue engineering scaffolds,” *Ann. Biomed. Eng.*, vol. 34, no. 1, pp. 89–101, 2006.

[8] H. Kaji, G. Camci-Unal, R. Langer, and A. Khademhosseini, “Engineering systems for the generation of patterned co-cultures for controlling cell-cell interactions,” *Biochim. Biophys. Acta*, vol. 1810, no. 3, pp. 239–250, 2011.

[9] G. P. M. Bissell , H. Glenn Hall, “How does the extracellular matrix direct gene expression?,” *J. Theor. Biol.*, vol. 99, no. 1, pp. 31–68, 1982.

[10] C. M. Nelson and M. J. Bissell, “Of Extracellular Matrix , Scaffolds , and Signaling : Tissue Architecture Regulates Development , Homeostasis , and Cancer,” *Annu. Rev. Cell Dev. Biol. 2006.*, vol. 22, no. 1, pp. 287–309, 2006.

[11] R. Xu, A. Boudreau, and M. J. Bissell, “Tissue architecture and function: Dynamic reciprocity via extra- and intra-cellular matrices,” *Cancer Metastasis Rev.*, vol. 28, no. 1–2, pp. 167–176, 2009.

[12] R. Perez-Castillejos, “Replication of the 3D architecture of tissues,” *Mater. Today*, vol. 13, no. 1–2, pp. 32–41, 2010.

[13] S. Chariklia, “Material processing via ultra-short pulsed laser : Study of the outgrowth and interfacing of neural networks in 3D Si scaffolds,” 2014.

[14] B. D. Ratner and S. J. Bryant, “Biomaterials: Where We Have Been and Where We Are Going,” *Annu. Rev. Biomed. Eng.*, vol. 6, no. 1, pp. 41–75, 2004.

[15] A. Ovsianikov *et al.*, “Laser fabrication of 3D gelatin scaffolds for the generation of bioartificial tissues,” *Materials (Basel).*, vol. 4, no. 1, pp. 288–299, 2010.

[16] X. H. & C. H. Lie , Changyou Gao , Zhengwei Mao , Jiacong Shen, “Thermal dehydration treatment and glutaraldehyde cross-linking to increase the biostability of collagen – chitosan porous scaffolds used as dermal equivalent,” *J. Biomater. Sci. Polym. Ed.*, vol. 14, no. 8, pp. 861–874, 2003.

[17] C. M. Murphy, M. G. Haugh, and F. J. O. Brien, “The effect of mean pore size on cell attachment, proliferation and migration in collagen–glycosaminoglycan scaffolds for bone tissue engineering,” *Biomaterials*, vol. 31, no. 3, pp. 461–466, 2010.

[18] T. M. Freyman, I. V Yannas, R. Yokoo, and L. J. Gibson, “Fibroblast Contractile Force Is Independent of the Stiffness Which Resists the Contraction,” *Exp. Cell Res.*, vol. 272, no. 2, pp. 153–162, 2002.

[19] E. Farrell *et al.*, “A Collagen-glycosaminoglycan Scaffold Supports Adult Rat Mesenchymal Stem Cell Differentiation Along Osteogenic and Chondrogenic Routes,” *Tissue Eng.*, vol. 12, no. 3, pp. 459–68, 2006.

[20] D. S. Torres, T. M. Freyman, I. V Yannas, and M. Spector, “Tendon cell contraction of collagen-GAG matrices in vitro: effect of cross-linking,” *Biomaterials*, vol. 21, no. 15, pp. 1607–1619, 2000.

[21] I. V. Yannas, D. S. Tzeranis, and B. A. Harley, “Biologically active collagen-based scaffolds : advances in processing and characterization,” *Philos Trans A Math Phys Eng Sci.*, vol. 368, no. 1917, pp. 2123–2139, 2010.

[22] F. J. O. Brien, B. A. Harley, I. V Yannas, and L. Gibson, “Influence of freezing rate on pore structure in freeze-dried collagen-GAG scaffolds,” *Biomaterials*, vol. 25, no. 6, pp. 1077–1086, 2004.

[23] S. Koo, S. M. Santoni, B. Z. Gao, C. P. Grigoropoulos, and Z. Ma, “Laser-assisted biofabrication in tissue engineering and regenerative medicine Sangmo,” 2017.

[24] Y. Liu, S. Sun, S. Singha, M. R. Cho, and R. J. Gordon, “3D femtosecond laser patterning of collagen for directed cell attachment,” *Biomaterials*, vol. 26, no. 22, pp. 4597–4605, 2005.

[25] V. Hovhannisyan, A. Ghazaryan, Y. Chen, S. Chen, and C. Dong, “Photophysical mechanisms of collagen modification by 80 MHz femtosecond laser,” *Opt. Express*, vol. 18, no. 23, pp. 24037–24047, 2010.

[26] O. Ilina, G. Bakker, A. Vasaturo, M. Hoffman, and P. Friedl, “Two-photon laser-generated microtracks in 3D collagen lattices: principles of MMP-dependent and -independent collective cancer cell invasion,” *Phys. Biol*, vol. 8, no. 2, 2011.

[27] A. Manickavasagam *et al.*, “Multimodal optical characterisation of collagen photodegradation by femtosecond infrared laser ablation,” *Analyst*, vol. 139, no. 23, pp. 6135–6143, 2014.

[28] O. Ilina, G.-J. Bakker, A. Vasaturo, R. M. Hoffman, and P. Friedl, “Two-photon laser-generated microtracks in 3D collagen lattices,” *Phys. Biol*, vol. 8, no. 2, 2011.

[29] J. Ma, B. F. Liu, Q. Y. Xu, and F. Z. Cui, “AFM study of hippocampal cells cultured on silicon wafers with nano-scale surface topograph,” *Colloids Surfaces B Biointerfaces*, vol. 44, no. 2–3, pp. 152–157, 2005.

[30] S. Gaspard, M. Forster, C. Huber, C. Zafiu, and M. Castillejo, “Femtosecond laser processing of biopolymers at high repetition rate,” *Phys. Chem.*, vol. 10, no. 40, pp. 6174–6181, 2008.

[31] K. Song, Z. Wang, R. Liu, G. Chen, and L. Liu, “Microfabrication-based three-dimensional (3-D) extracellular matrix microenvironments for cancer and other diseases,” *Int. J. Mol. Sci.*, vol. 19, no. 4, 2018.

[32] K. C. Hribar, K. Meggs, J. Liu, W. Zhu, X. Qu, and S. Chen, “Three-dimensional direct cell patterning in collagen hydrogels with near-infrared femtosecond laser,” *Sci. Rep.*, vol. 5, no. 17203, pp. 1–7, 2015.

[33] C. H. LEE, Y. C. LIM, D. F. FARSON, H. M. POWELL, and J. J. LANNUTTI, “Vascular Wall Engineering Via Femtosecond Laser Ablation : Scaffolds with Self-Containing Smooth Muscle Cell Populations,” *Ann. Biomed. Eng.*, vol. 39, no. 12, pp. 3031–3041, 2011.

[34] D. Bäuerle, *Laser Processing and Chemistry*, vol. 1, no. 9. 2011.

[35] S. K. Sundaram and E. Mazur, “Inducing and probing non-thermal transitions in semiconductors using femtosecond laser pulses,” *Nat. Mater.*, vol. 1, no. 4, pp. 217–224, 2002.

[36] Z. M. Sangmo Koo, Samantha M. Santoni, Bruce Z. Gao, Costas P. Grigoropoulos, “Laser-assisted biofabrication in tissue engineering and regenerative medicine,” *Mater. Res. Soc.*, vol. 32, no. 1, pp. 128–142, 2017.

[37] M. S. Brown and C. B. Arnold, “Laser Precision Microfabrication,” in *Springer Series in Materials Science*, vol. 135, no. 4, 2010, pp. 91–120.

[38] E. Stratakis, A. Ranella, M. Farsari, and C. Fotakis, “Laser-based micro/nanoengineering for biological applications,” *Prog. Quantum Electron.*, vol. 33, no. 5, pp. 127–163, 2009.

[39] C. Phipps, *Laser Ablation and its Applications*. 2007.

[40] A. Vogel and V. Venugopalan, “Mechanisms of pulsed laser ablation of biological tissues,” *Chem. Rev.*, vol. 103, no. 2, pp. 577–644, 2003.

[41] D. S. Tzeranis, “Imaging Studies of Peripheral Nerve Regeneration Induced by Porous Collagen Biomaterials by,” 2013.

[42] N. Garcia, Almudena; Fernández, Eva; Cortadellas, *Biomedical and Biological Applications of Scanning Electron Microscopy*. 2012.

[43] James J. Norman and T. A. Desai, “Control of Cellular Organization in Three Dimensions,” *Tissue Eng.*, vol. 11, no. 3, pp. 378–387, 2005.

[44] R. G. Harrison, “The Reaction Of Embryonic Cell To Solid Structures,” *J. Exp. Zool. banner*, vol. 17, no. 4, pp. 521–544, 1901.

[45] J. P. Kaiser, A. Reinmann, and A. Bruinink, “The effect of topographic characteristics on cell migration velocity,” *Biomaterials*, vol. 27, no. 30, pp. 5230–5241, 2006.

[46] F. L. Mi, S. S. Shyu, Y. B. Wu, S. T. Lee, J. Y. Shyong, and R. N. Huang, “Fabrication and characterization of a sponge-like asymmetric chitosan membrane as a wound dressing,”

Biomaterials, vol. 22, no. 2, pp. 165–173, 2001.

[47] R. H. Cholas, H. P. Hsu, and M. Spector, “The reparative response to cross-linked collagen-based scaffolds in a rat spinal cord gap model,” *Biomaterials*, vol. 33, no. 7, pp. 2050–2059, 2012.

[48] M. Hatami *et al.*, “Human embryonic stem cell-derived neural precursor transplants in collagen scaffolds promote recovery in injured rat spinal cord,” *Cytotherapy*, vol. 11, no. 5, pp. 618–630, 2009.

[49] N. R. Cashman *et al.*, “Neuroblastoma × spinal cord (NSC) hybrid cell lines resemble developing motor neurons,” *Dev. Dyn.*, vol. 194, no. 3, pp. 209–221, 1992.

[50] J. A. Laib, J. A. Marin, R. A. Bloodgood, and W. H. Guilford, “The reciprocal coordination and mechanics of molecular motors in living cells.,” *Proc. Natl. Acad. Sci.*, vol. 106, no. 9, pp. 3190–5, 2009.

[51] Y. Kang and J. Chang, “Channels in a porous scaffold: A new player for vascularization,” *Regen. Med.*, vol. 13, no. 6, pp. 705–715, 2018.

[52] J. Rouwkema and A. Khademhosseini, “Vascularization and Angiogenesis in Tissue Engineering: Beyond Creating Static Networks,” *Trends Biotechnol.*, vol. 34, no. 9, pp. 733–745, 2016.